

Department of Physics and Astronomy
University of Heidelberg

Bachelor Thesis in Physics
submitted by

Marco Zimmermann

born in Lörrach (Germany)

August 21, 2012

Cooling with Gaseous Helium for the Mu3e Experiment

This Bachelor Thesis has been carried out by

Marco Zimmermann

at the

Institute of Physics

under the supervision of

Prof. Dr. André Schöning

Abstract

An experimental setup to investigate cooling by forced convection with gaseous helium was developed and characterized. This gives insight on the cooling in the detector for the Mu3e-experiment which intends to search for the lepton flavour violating decay $\mu^+ \rightarrow e^+ e^+ e^-$. A sensitivity of one decay in 10^{16} muon decays is aspired whereas according to the standard model of particle physics, this decay is even much more suppressed. A $\mu^+ \rightarrow e^+ e^+ e^-$ signal event would be a clear sign of physics beyond the Standard Model. To achieve such a high sensitivity, new High Voltage Monolithic Active Pixel Sensors (HV-MAPS) are used. The expected heat dissipation is about 100 mW/cm^2 . The cooling is intended to be achieved by a constant helium gas flow along the pixel sensor layers.

The experimental setup includes an induction heating to simulate the heat generation in the sensor. The sensor is replaced by a probe consisting of aluminium, Kapton[®] and silicon orientated on the detector design. This probe is positioned inside a specially developed box that contains temperature sensors and gas connectors.

First measurement results are compared to theoretical predictions and to a numerical simulation. Both the measurements and the predictions show that the maximum sensor temperature is observed at maximal distance to the gas inlet and it is proportional to the heat output. With constant helium flow, a thermal steady-state is observed after some seconds. The sensor temperature reaches (depending on starting temperature) up to $65 \text{ }^\circ\text{C}$ with the expected heat dissipation and a helium flow of $0.165 \frac{\text{L}}{\text{s}}$ at room temperature.

Zusammenfassung

Ein Versuchsaufbau zur Untersuchung der Kühlung durch erzwungene Konvektion mit gasförmigem Helium wurde entwickelt und untersucht. Diese Experimente bieten Aufschlüsse zur Konzeption der Kühlung im Detektor für das geplante Mu3e-Experiment. Dieses soll nach dem leptonenzahlverletzenden Zerfall $\mu^+ \rightarrow e^+ e^+ e^-$ mit einer Sensitivität von einem in 10^{16} Myon-Zerfällen suchen. Der Zerfall ist im Standardmodell der Teilchenphysik weit unter dieser Sensitivität unterdrückt; jedes $\mu^+ \rightarrow e^+ e^+ e^-$ Signal wäre ein eindeutiges Zeichen für Physik jenseits des Standardmodells. Um diese hohe Sensitivität zu erreichen, werden neuartige Monolithisch Aktive Hochspannungspixelsensoren (HV-MAPS) zur Teilchendetektion verwendet. Die erwartete Wärmeleistung beträgt etwa 100 mW/cm^2 . Die Kühlung soll durch einen konstanten Heliumgasstrom entlang der Pixelsensoren erreicht werden.

Der Versuchsaufbau beinhaltet eine Induktionsheizung, um die Wärmeerzeugung im Sensor zu simulieren. Der Sensor wird durch ein Probenstück aus Aluminium, Kapton[®] und Silizium ersetzt, das sich am Detektordesign orientiert. Das Probenstück wird in einer speziell entwickelten Box, die Temperatursensoren und Gasanschlüssen enthält, befestigt.

Erste Messergebnisse wurden mit theoretischen Vorhersagen sowie einer numerischen Strömungssimulation verglichen. Sowohl die Messungen als auch die Vorhersagen zeigen, dass die maximale Sensortemperatur bei größtmöglicher Entfernung zum Gaseinlass erreicht wird und proportional zur Wärmeleistung ist. Bei konstantem Heliumgasstrom stellt sich zudem bereits nach einigen Sekunden ein thermisches Gleichgewicht ein. Die Sensortemperatur erreicht bei der erwarteten Heizleistung und einem Heliumfluss von $0.165 \frac{\text{L}}{\text{s}}$ auf Raumtemperatur (abhängig von der Starttemperatur) bis zu $65 \text{ }^\circ\text{C}$.

Contents

| | |
|---|------------|
| Abstract | i |
| List of Figures | v |
| List of Tables | vii |
| 1. Introduction | 1 |
| 2. The Mu3e Experiment | 3 |
| 2.1. Physical Motivation | 3 |
| 2.2. Detector Design | 4 |
| 3. Experimental Setup | 7 |
| 3.1. Cooling Setup Design and Flow Measurement Devices | 7 |
| 3.2. Inductive Heating | 10 |
| 3.2.1. Royer Converter | 11 |
| 3.2.2. Dimensioning of the Components | 13 |
| 3.3. Readout of Temperature Data | 16 |
| 4. Theory and Simulation of Heat Transfer by Forced Convection | 21 |
| 4.1. Laminar Gas Flow over a Flat Solid Surface | 22 |
| 4.1.1. Analytical Description of Heat Transfer | 22 |
| 4.1.2. Calculations for the Experimental Setup | 27 |
| 4.2. Simulation of Heat Transfer by Forced Convection around 50 μm Silicon Layer . | 30 |
| 5. Measurements | 37 |
| 5.1. Preparative Measurements | 37 |
| 5.2. Cooling Measurements | 44 |
| 5.3. Discussion of Systematic Errors | 52 |
| 6. Discussion and Outlook | 53 |
| Bibliography | 57 |
| Acknowledgements | 59 |
| A. LabView programming for temperature readout | 61 |

List of Figures

| | |
|---|----|
| 2.1. Mu3e logo | 3 |
| 2.2. Feynman diagrams for the decay $\mu^+ \rightarrow e^+ e^+ e^-$ | 4 |
| 2.3. Schematic of Mu3e detector baseline design | 5 |
| 2.4. Model of mechanics and prototype for the Mu3e detector | 6 |
| 3.1. Setup to produce laminar gas flow past a flat surface, including induction coil and temperature sensors | 8 |
| 3.2. Rotameters for flow measurements | 9 |
| 3.3. Lorentzian function as an approximation for the resonance curve of a harmonic oscillation near the resonant frequency ω_0 | 10 |
| 3.4. Wiring diagram of the induction heating | 11 |
| 3.5. Simulated voltage and current signals | 12 |
| 3.6. Oscilloscope measurement of voltages in the Royer oscillator | 13 |
| 3.7. Constructed induction heating | 14 |
| 3.8. Measurement of heating for different oscillating frequencies | 15 |
| 3.9. Safe operating area of the transistor BUV27G | 16 |
| 3.10. Temperature-resistance curve for the pt1000 sensors | 17 |
| 3.11. Connections for temperature data readout | 18 |
| 3.12. Exemplary calibration of an ADC channel | 19 |
| 4.1. Sketch of the boundary layer over a flat solid surface | 23 |
| 4.2. Velocity profile of a laminar boundary layer | 24 |
| 4.3. Theoretical prediction on helium flow velocity u_∞ for different boundary conditions | 29 |
| 4.4. Geometry and coordinate system of the CFD simulation | 30 |
| 4.5. Heat conductivity of silicon empirically given and linearly approximated | 31 |
| 4.6. Exemplary temperature profiles obtained in the CFD simulation | 32 |
| 4.7. Temperature profiles on the silicon sensor for different initial helium temperatures | 33 |
| 4.8. Silicon layer temperature and vertical helium temperature | 34 |
| 4.9. Simulated maximum silicon temperature for different initial flow speed values | 35 |
| 5.1. Measurement of self heating without induction heating or gas flow | 37 |
| 5.2. Measurement of temperature increase by inductively produced heat inside the pt1000 sensor | 38 |
| 5.3. Measurement of temperature sensor response time | 39 |
| 5.4. Measurement of heating temperature gradient | 41 |
| 5.5. Efficiency of the induction heating | 42 |

List of Figures

| | |
|--|----|
| 5.6. Cooling of aluminium foil inside the cooling box without forced convection . . . | 43 |
| 5.7. Measurement of helium temperature | 44 |
| 5.8. Temperature profile in cooling measurement varying helium volume flow | 45 |
| 5.9. Difference between measured temperature and room temperature for different volume flow values | 46 |
| 5.10. Gas outlet, pt1000 sensors and silicon surface layout for cooling measurement . | 47 |
| 5.11. Difference between measured silicon temperature and room temperature for different helium flow and position on the sample | 49 |
| 5.12. Temperature profile in cooling measurement varying power input | 50 |
| 5.13. Difference between measured temperature and room temperature for different power input values | 51 |
| A.1. User interface of the used temperature readout program | 61 |
| A.2. LabView programming (excerpt) | 62 |

List of Tables

| | |
|--|----|
| 4.1. Some thermophysical properties of helium and air | 28 |
| 4.2. Calculated results for the free fluid stream velocity u_{∞} for helium and air in the experimental setup | 28 |
| 4.3. Calculated boundary layer thicknesses at $x = L$ and the corresponding helium volume gas flow for different boundary conditions | 29 |
| 5.1. Density and specific heat capacity of silicon, aluminium and Kapton [®] | 41 |
| 5.2. Theoretical temperature difference predictions | 48 |
| 5.3. Helium and silicon power input | 51 |

1. Introduction

Several experiments are currently performed or planned to search for new physics beyond the Standard Model (SM) of elementary particle physics, e.g. at the Large Hadron Collider (LHC). The SM is today the basis of elementary particle physics and describes the properties of particles and their interactions. Since the SM implicates the conservation of lepton flavour at tree level, a measurement of a lepton flavour violating decay would be a clear sign of new physics. The missing unification with gravity, the observed lepton flavour violation in the form of neutrino mixing and other existing open questions indicate that the SM can not be considered as a *complete* theory of elementary particle physics. Theories giving explanations on open questions in the SM predict new phenomena at high mass scales that have not been proven yet.

The Mu3e experiment intends to search for the lepton flavour violating decay $\mu^+ \rightarrow e^+ e^+ e^-$. The detection of this decay is planned to be performed by achieving a high sensitivity of one decay in about 10^{16} muon decays. This sensitivity requires muon intensities in excess of 10^9 muons per second [1]. The experiment will therefore take place at the Paul Scherrer Institute (PSI) at an upgraded beamline. A high granularity and a low material budget in order to reduce multiple scattering are necessary for precision tracking and vertexing. Therefore, a detector design consisting of new High Voltage Monolithic Active Pixel Sensors (HV-MAPS) thinned to $50 \mu\text{m}$ and supported by a Kapton[®] frame is developed.

The heat output of the pixel sensors is expected to be about $100 \text{ mW}/\text{cm}^2$. Cooling is required and proposed to be achieved by a constant helium gas flow. In this thesis, the development of an experimental setup allowing studies on this cooling design is described. The experimental setup includes an induction heating in order to simulate the heat generation in the sensor and enables a contactless power transmission. It is dimensioned to achieve the expected heat output of the actual MAPS used in the detector. The sensor is replaced by a probe consisting of aluminium, Kapton[®] and silicon. The Kapton[®] and silicon are orientated on the detector design whereas the aluminium is heated by the induction heating. The probe is positioned inside a specially developed box that contains temperature sensors and gas connectors. In addition to the experimental part, some theoretical calculations and a numerical simulation based on fluid dynamics are performed that can be compared to measurements with the experimental setup.

A short introduction into the Mu3e experiment is given in chapter 2, before the setup developed for experimental cooling studies is described in chapter 3. The theoretical part including analytical calculations and a numerical simulation based on fluid dynamics follow in chapter 4. In chapter 5, the experimental setup is characterized in order to perform first cooling measurements that are compared to the theoretical predictions. They are concluded in chapter 6 with a comparison of the measurement results and the theoretical predictions and with an outlook on further measurements and optimizations.

2. The Mu3e Experiment

The Mu3e experiment intends to search for the lepton flavour violating decay $\mu^+ \rightarrow e^+ e^+ e^-$. The search for this rare and forbidden¹ decay requires very precise measurements. Former measurements of the SINDRUM collaboration² did not find any signal event for this decay and set the branching ratio limit $\text{BR}(\mu^+ \rightarrow e^+ e^+ e^-) < 1 \times 10^{-12}$ [2]. The Mu3e experiment aims a branching ratio sensitivity of 10^{-16} at 90% confidence level [1].

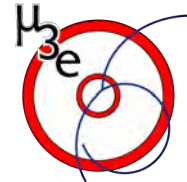


Figure 2.1.
Mu3e logo

2.1. Physical Motivation

In the Standard Model (SM) of elementary particle physics, the number of leptons of each family (lepton flavour) is a conserved quantity at tree level. The main μ^+ decay channel is $\mu^+ \rightarrow e^+ \nu_e \bar{\nu}_\mu$ with a branching ratio of almost 100% and is lepton flavour conserving. Other decays with additional photons and electrons are $\mu^+ \rightarrow e^+ \nu_e \bar{\nu}_\mu \gamma$ with a branching ratio of $1.4(4) \times 10^{-2}$ and $\mu^+ \rightarrow e^+ e^+ e^- \nu_e \bar{\nu}_\mu$ with a branching ratio of $3.4(4) \times 10^{-5}$ [3].

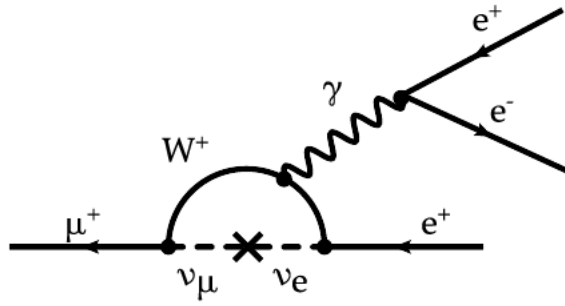
In the ν SM, an extension of the SM, only the number of leptons regardless of the generation is conserved. It allows lepton flavour violations via neutrino oscillation [5] which have been experimentally observed [4]. However, the ν SM decay $\mu^+ \rightarrow e^+ e^+ e^-$ based on neutrino mixing is greatly suppressed with a branching ratio $\approx 10^{-50}$. The feynman graph for such a decay is shown in figure 2.2a. The identification of a $\mu^+ \rightarrow e^+ e^+ e^-$ decay with a branching ratio inside the projected experimental range of the Mu3e experiment would therefore be a clear sign of new physics.

Beside observed lepton flavour violation via neutrino oscillations, other open questions concerning e.g. the unification of gravity or the neutrino mass exist and motivate the search for physics beyond the SM. There are several theories beyond the SM predicting new phenomena such as lepton flavour violating processes. Supersymmetric models predict lepton flavour violation in an experimentally accessible amount [1]. Figure 2.2b shows a feynman graph involving supersymmetric particles (SUSY model). The mixing particles in the loop are sleptons and the additional neutral particle is a neutralino [6].

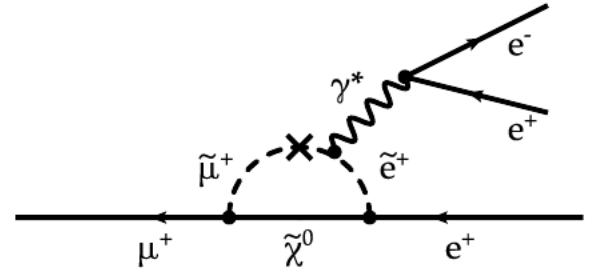
Other predicted lepton flavour violating decays are $\mu^+ \rightarrow e^+ \bar{\nu}_e \nu_\mu$ with an experimental limit at 90% confidence level $< 1.2 \times 10^{-2}$, $\mu^+ \rightarrow e^+ \gamma$ with experimental limit (90% conf. lev.) $< 2.4 \times 10^{-12}$ and $\mu^+ \rightarrow e^+ 2\gamma$ (exp. limit $< 7.2 \times 10^{-11}$ at 90% conf. lev.) [3].

¹in the Standard Model

²The SINDRUM experiment was running at the Paul Scherrer Institut from 1983 to 1986.



(a) The Standard Model loop-level diagram.



(b) A diagram involving supersymmetric particles [6].

Figure 2.2.

Feynman diagrams for the decay $\mu^+ \rightarrow e^+ e^+ e^-$.

2.2. Detector Design

The projected sensitivity of 10^{-16} requires muon intensities in excess of 10^9 muons per second in order to obtain a sufficient number of events. This intensity is currently planned to be available with an upgraded muon beamline after 2017 at the PSI³ [1]. The muon beam is stopped in a hollow aluminium double cone target shown in figure 2.3. According to simulations, about 90% of the muons are stopped in the target with a wall thickness of about $40 \mu\text{m}$ to $70 \mu\text{m}$. Assuming a muon stopped in the target decays at rest, the vectorial sum of momenta of the decay products has to vanish

$$\left| \sum_{i=1}^3 p_i \right| = 0. \quad (2.1)$$

The invariant mass of the decay products at the vertex is always identical to the muon mass:

$$\left(\sum_{i=1}^3 P_i \right)^2 = m_\mu^2 c^4. \quad (2.2)$$

The trajectories of the decay products are therefore in one plane and the energy of the decay products is limited to half of the muon mass ($\approx 53 \text{ MeV}/c^2$).

The high muon beam intensity requires a very fast detector for the decay products. The suppression of accidental background signals requires a very high vertex and time resolution. Accidental background signals originate from random coincidences of electron and positron tracks produced in independent events. The separation of $\mu^+ \rightarrow e^+ e^+ e^- \nu_e \bar{\nu}_\mu$ and $\mu^+ \rightarrow e^+ e^+ e^-$ events requires a very high momentum resolution. The additional neutrinos in the background signal decay cannot be detected, but need to be considered in equations 2.1 and 2.2. In opposite to the $\mu^+ \rightarrow e^+ e^+ e^-$ decay, these equations are therefore not valid for the three charged particles in the back-

³Paul Scherrer Institut, Viligen, Switzerland

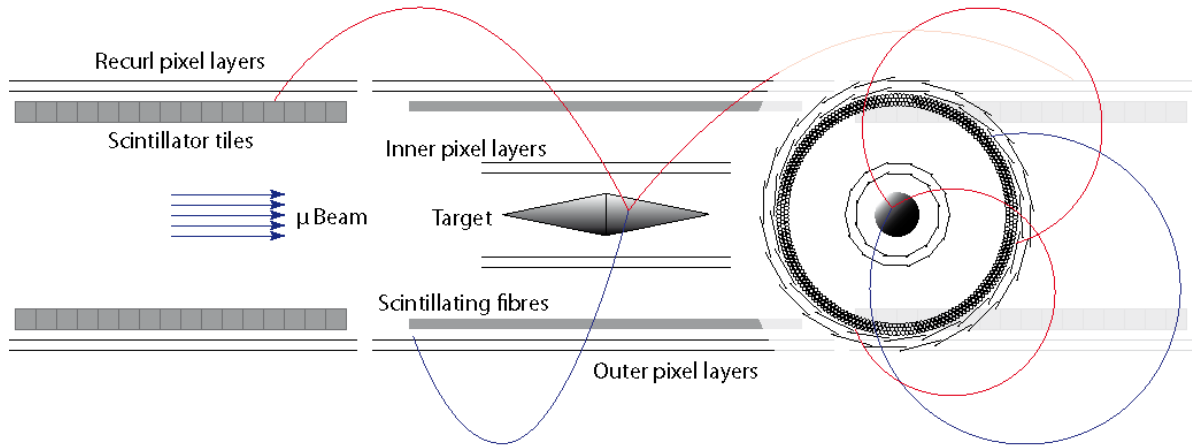


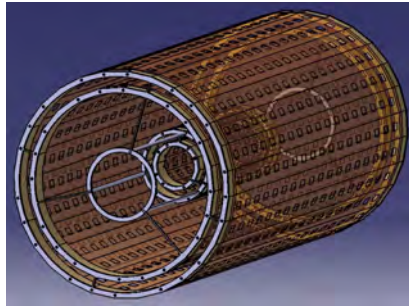
Figure 2.3.
Schematic of Mu3e detector baseline design (not to scale). Side view on the left and transverse view on the right.

ground decay separately. Multiple scattering effects are the dominating source of measurement uncertainties [7] and therefore the material budget needs to be minimized.

Those requirements lead to the decision to use new High Voltage Monolithic Active Pixel Sensors (HV-MAPS). This technology integrates sensor and readout functionalities in the same device and thus greatly reduces the material budget. It provides a high granularity and a timing information better than 100 ns [1] since charge collection is achieved by drift in an electric field instead of diffusion. The pixel sensors are supported by a framework mainly consisting of 25 μm thick Kapton[®] foil arranged in a polygonal form. Two concentric double layers of pixel sensors provide tracking informations. A schematic of the baseline detector design can be seen in figure 2.3. The red and blue lines represent typical particle tracks. The current detector design consists of two more recurl stations upstream and downstream (five instead of three detector segments with 36 cm length as shown in figure 2.3).

The occupancy is highest for the inner detector layer, which should be placed as close as possible to the target to provide precise vertex position information. The signal rate at the inner most layer is at most 3 kHz per channel for a muon stop rate of 2×10^9 muons/s [1]. The total number of pixels is about 250×10^6 (depending on the actual number of recurl stations) for a pixel size of $80 \mu\text{m} \times 80 \mu\text{m}$ [1]. The use of pixel sensors and the high signal rate lead to an expected heat output of about $100 \text{ mW}/\text{cm}^2$. The required cooling is intended to be achieved by a helium gas flow in axially direction. Gaseous helium is used because of its low atomic number, its very low chemical reactivity and its in comparison to other gases high thermal conductivity. A laminar gas flow is envisaged in order to reduce mechanic forces on the Kapton[®] framework. Studies on this cooling design are the subject of this thesis.

In figure 2.4, a three-dimensional model of the inner and outer pixel layers together with a prototype of the inner pixel layers are shown to illustrate the detector layout. One sensor layer consists of 25 μm Kapton[®] foil, 25 μm flex print and 50 μm silicon of the MAPS. The helium gas flow is planned to be applied in axial direction along the sensor surfaces.



(a) Model of mechanics for inner and outer pixel layers.



(b) Prototype of inner layers. The silicon pixel sensors are replaced by glass.

Figure 2.4.

Three-dimensional model of mechanics of one detector segment and prototype of pixel layers for the Mu3e detector.

Additional timing information is provided by scintillating tiles and fibres. They are installed just before the outer double pixel layers as it can be seen in figure 2.3. The whole setup is placed a solenoidal magnetic field B of about 1 T to 1.5 T [1] leading to curved charged particle tracks.

3. Experimental Setup

The experimental setup is designed to investigate the cooling of a heated surface by a helium gas flow. In order to exclude thermal conduction via connection wires, this surface is intended to be heated inductively. In this chapter, the development and configuration of the experimental setup are explained. This development is divided into three parts: The inductive heating, the readout of temperature data and the cooling box in which all parts are installed in order to observe the cooling by forced convection.

3.1. Cooling Setup Design and Flow Measurement Devices

In this section, the development of a setup to provide a laminar gas flow over a heated sample is described. The sample consists of Kapton[®] foil, aluminium foil and silicon layered on top of each other. The Kapton[®] foil and the silicon correspond to the final detector design, whereas the aluminium foil is needed as a conductive material that can be heated inductively. The dimensions of the sample are about $85 \times 25\text{mm}^2$. The silicon layer used for this cooling studies has a thickness of $500\ \mu\text{m}$ although the silicon layer thickness inside the detector is planned to be only $50\ \mu\text{m}$. This thicker silicon was chosen because a thin silicon wafer is very difficult to be cut to the proper dimensions. The heat conductivity of the different materials is discussed in the following chapter.

The setup to provide the gas flow has to provide space for the primary coil of the induction heating. The ratio of the sample area and the area inside the coil must be maximized to achieve sufficient heating. As a result of that, it was decided to use a cornered coil to heat the rectangular sample. Tests performed with the induction heating described in the following subsection showed that the coil shape does not influence the voltage signal shape inside the coil. Furthermore, the flowing gas should be thermally shielded and direct contact of the sample to the surrounding material must be minimized because of thermal conduction. However, direct contact is not completely omissible due to the need of mechanic fixture that exists because of shear stress caused by the gas flow. Moreover, all electroconductive material inside the coil is heated inductively which distorts temperature measurements. Nevertheless, the temperature readout is intended to be done with pt1000 sensors (see section 3.3) that need to be wired. In fact, the resulting self heating must be measured and considered while evaluating heating and cooling of the sample.

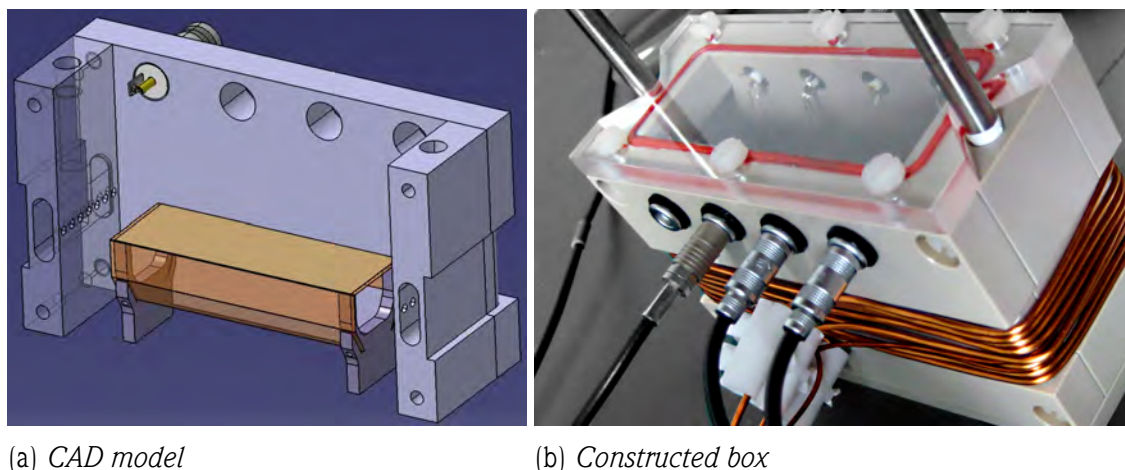


Figure 3.1.

Setup to produce laminar gas flow past a flat surface, including induction coil and temperature sensors

Figure 3.1 shows the setup that was designed considering these constraints. The picture on the left hand side shows the computer-aided design (CAD) model used for the construction and the right one the constructed box. The CAD model contains the originally designed dimensions of the sample $6 \times 2\text{cm}^2$. It was intended to provide 1 cm space between gas inlet and sample considering possibly arising turbulent flow directly at the inlet. Unfortunately, the resulting and previously mentioned area ratio considering the area inside the coil became too small to heat the sample. Consequently, the sample dimensions were adjusted to $8.5 \times 2.5\text{cm}^2$. The contact between the sample and any other parts is reduced to a minimum. Indeed, there are only four direct contact points of the whole sample. Moreover, the Kapton[®] foil is cut larger than the rest of the sample and fixed with nylon screws. This mechanical fixture takes into account the low thermal conductivity of Kapton[®] which is 0.12 W/m K [8].

The walls of the box are made of Polyetheretherketone (PEEK) which is a heat-resistant thermoplastic (heat conductivity 0.25 W/m K [9]). The lemo connectors for the temperature sensors consist of electroconductive material and are therefore placed 1 cm above the coil expecting that the resulting longer wires do not produce as much heat. The lemo cables visible in figure 3.1 connect the pt1000 sensors to a current source (see section 3.3). To avoid even more electroconductive material, nylon screws are used instead of metallic ones. The coil position made it necessary to let the gas flow from the top into the cooling box and exit in the same way on the other side.

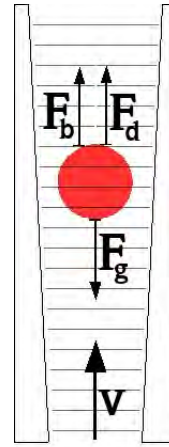
The gas flow setup is completed by rotameters connected to a gas cylinder on one side and the entry of the cooling box on the other side via silicone hose. It is evident that the gas volume flow defining the gas velocity is one of the parameters that specify the actual cooling effect and therefore needs to be measured. The measurements are made using helium to investigate the cooling effect that can be expected in the detector and with nitrogen to compare the cooling effect and because of cost concerns.

The rotameters can be seen in figure 3.2. They consist of a tapered glass tube and a spheri-

cal weight (float). They must be vertically orientated and connected so that the gas is flowing upwards through the glas tube. ¹



(a) Image of rotameters



(b) Schematic design of a rotameter including occuring forces [11]

Figure 3.2.
Rotameters for flow measurements

Each flowmeter must be calibrated for the gas measured. Since the flowmeters used were initially calibrated for other gases used in former measurements, a recalibration had to be done. This was performed using software provided by the manufacturing company ABB (originally Fischer&Porter). Each flowmeter is only usable inside a particular volume flow range depending on the gas characteristics (especially gas density). The flowmeter connected to the helium gas cylinder allows a volume flux from $8.4 \frac{\text{mL}}{\text{s}}$ up to $0.25 \frac{\text{L}}{\text{s}}$, the one connected to nitrogen from $0.125 \frac{\text{L}}{\text{s}}$ up to $1.25 \frac{\text{L}}{\text{s}}$. The cooling with helium gas flow is expected to be more effective than

¹There are three forces acting on the weight inside the tube: drag force and buoyant force are orientated upwards whereas the gravity force points in the opposite direction. The drag force F_d depends on the flow speed v squared: [10]

$$F_d \propto A_f \cdot \rho_g \cdot v^2 \quad (3.1)$$

A_f = cross sectional area of the float

ρ_g = gas density

whereas buoyant force F_b and gravitational force F_g are independent of the volumetric gas flow:

$$F_g \propto V_f \cdot \rho_f \cdot g \quad (3.2)$$

$$F_b \propto V_f \cdot \rho_g \cdot g \quad (3.3)$$

V_f = volume of the float

ρ_f = density of the float

g = local acceleration due to gravity

The flow speed increases with higher volumetric flow rate, however, the widening of the cone shaped tube causes a decreasing flow velocity until there is an equilibrium state in which all forces cancel. Consequently, the heighth of the float is a measurement of the volumetric flow rate and can be read on a scale on the glas tube.

with nitrogen, thus the nitrogen flowmeter is dimensioned larger. The expected volume flow ranges rely on the calculations performed in chapter 4.

3.2. Inductive Heating

The heating is dimensioned to heat the sample with a heat input of about 100 mW/m^2 . An inductive heating is chosen because it allows a contactless power transmission. The heating is achieved by eddy currents within the sample, which explains the need of the aluminium as a conductive material. Using a ferromagnetic material such as iron would have the advantage of additional magnetic hysteresis losses, but aluminium foil is commercially available. The alternating electromagnetic field generating these eddy currents is produced by an oscillating circuit mainly consisting of a capacity and an inductor. For frequencies near the resonant frequency ω_0 , the resonance curve of a harmonic oscillation can be approximated by a symmetric lorentzian curve in the form

$$I(\omega) = A^2(\omega) \propto \frac{\left(\frac{\Gamma}{2}\right)^2}{(\omega - \omega_0)^2 + \left(\frac{\Gamma}{2}\right)^2} \quad (3.4)$$

The linewidth of the resonance, Γ , depends on the damping of the oscillation and is antiproportional to the quality factor Q .

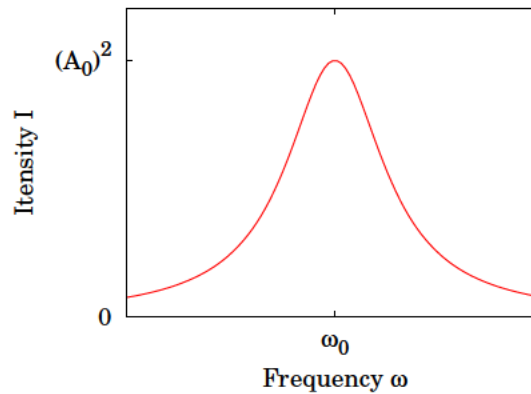


Figure 3.3.

Lorentzian function as an approximation for the resonance curve of a harmonic oscillation near the resonant frequency ω_0

tional to the quality factor Q . Figure 3.3 shows the resonance curve of a harmonic oscillation according to equation 3.4. For a LC-circuit, the resonant frequency is

$$\omega_0 = \frac{1}{\sqrt{LC}}. \quad (3.5)$$

It can be seen that the amplitude decreases very quickly with increasing difference $(\omega - \omega_0)$. Consequently, if an LC-circuit is driven by an AC voltage with a different frequency than the

resonant frequency ω_0 , power dissipation will increase considerably. It is therefore reasonable to drive the harmonic oscillation at the resonant frequency ω_0 . This is no problem as long as ω_0 can be calculated according to equation 3.5 and is therefore known. However, the capacity C and the inductance L may slightly change because of temperature changes or aging. Furthermore, the resonant frequency changes if power is transmitted to a secondary oscillating circuit (which is in this experiment represented by the aluminium foil). That is why it is difficult to predict the resonant frequency precisely. In spite of this fact, an oscillating circuit that is always in resonance to minimize power dissipations is feasible and explained in the following subsection.

3.2.1. Royer Converter

An oscillating circuit that is always in resonance is realized using a so-called *Royer Converter*². Similar set-ups are used for charging stations of toothbrushes. Figure 3.4 shows the wiring diagram of the developed induction heating.

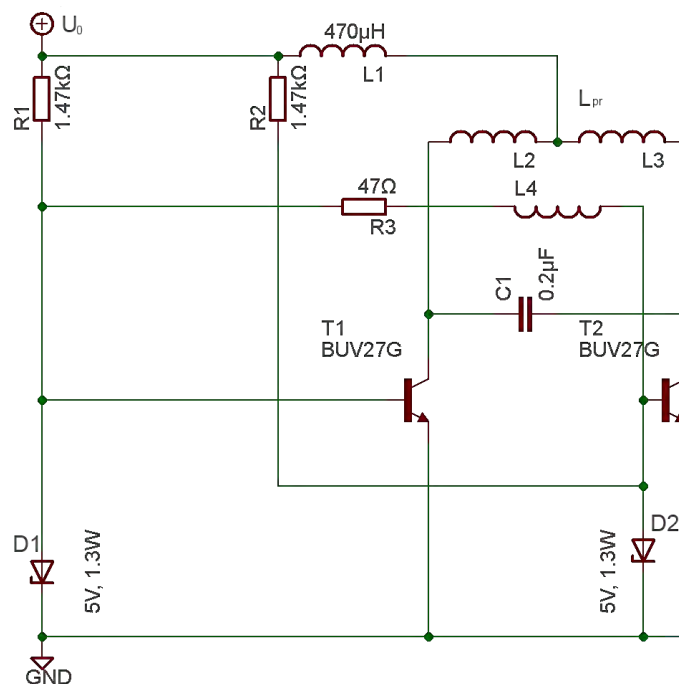


Figure 3.4.
Wiring diagram of the induction heating

The LC-circuit which heats the sample inside the cooling box consists of the capacity $C1$ and the center-tapped inductor L_{pr} . The two halves of L_{pr} are labeled $L2$ and $L3$. Therefore the oscillation frequency is determined by L_{pr} and $C1$. The choke $L1$ ensures that the center tap is alternating voltage wise decoupled from the constant operating voltage U_0 . The choke must not

²The original schematic was developed by George Howard Royer in 1954 with a rectangular output signal (no capacity). The circuit used for the induction heating goes back to Peter James Baxandall.[12]

3. Experimental Setup

go into saturation and must therefore be at least three times higher than L_{pr} , but a higher value is even better.

The transistors $T1$ and $T2$ are connected in push-pull operation which means that they switch alternately so that current flows alternating through $L2$ or $L3$. They are controlled by the feedback winding $L4$ which gains its signal from the primary winding L_{pr} . Consequently, the circuit is self-regulating and the oscillation is always resonant. The transistors switch in the zero-crossing of the sinusoidal voltage. The zener diodes $D1$ and $D2$ were added to limit the applied voltage to the bases of the transistors, the resistor $R3$ limits the current through the diodes. The resistors $R1$ and $R2$ connecting the bases of the transistors to the constant voltage source enable the transient oscillation and dissipate current from the control winding.

The voltage signal in the primary coil equals a half-wave rectified sine. The amplitude U_{pr} can be calculated considering the ratio of peak value to arithmetic mean value of this wave form leading to

$$U_{pr} = \pi U_0. \quad (3.6)$$

The peak current I_{pr} in the LC-circuit is then obtained by

$$I_{pr} = U_{pr} \cdot \sqrt{\frac{L}{C}} = \pi U_0 \cdot \sqrt{\frac{C}{L}}. \quad (3.7)$$

The circuit shown in figure 3.4 was simulated with LTSpice. This facilitates the dimensioning of the components since changes can be tested in the simulation first. Figure 3.5 shows the simulated voltage signal U_{pr} at both halves of the primary inductance L_{pr} (blue lines), U_{st} at the bases of the transistors (green and magenta lines) and the current I in the LC-circuit (red line) for $U_0 = 8.5 \text{ V}$. In no-load running, the current is 90° phase shifted to the primary coil voltage. A slight deviation results from the power transmitted to the control winding.

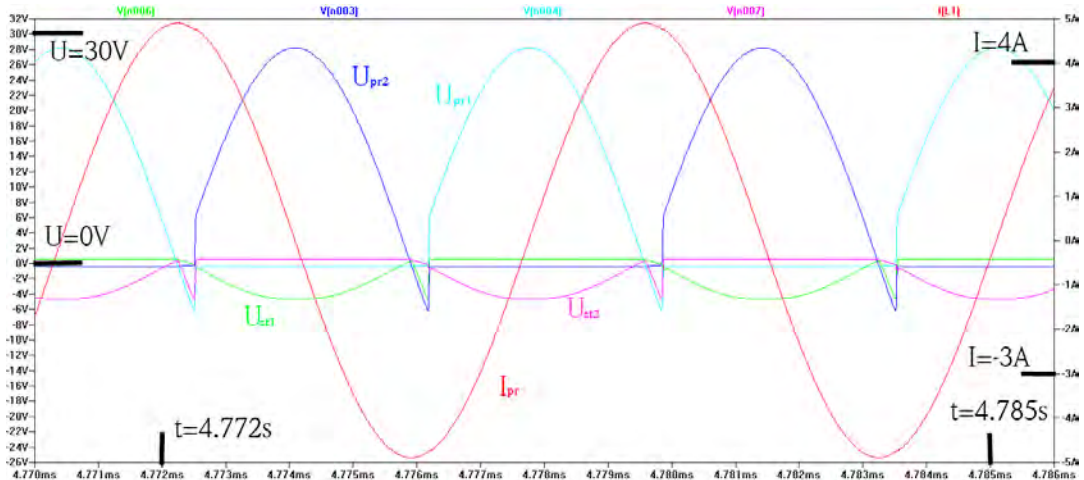


Figure 3.5.
Simulated voltage and current signals

The simulated peak voltage U_{pr} is about (1 – 2)V higher than calculated in equation 3.6 which results from the short negative peak directly after the positive half sine peak. This effect can be observed as well in the experiment which can be seen in figure 3.6. The perturbation effects observed in the voltage signal at the control winding (see fig. 3.6b) are much larger than at the primary coil (fig. 3.6a) and in the simulation (fig. 3.5). However, this is not problematic as long as the primary coil voltage signal is mostly unaffected. An improvement of the control winding voltage signal would be achievable by adding more control windings to get a better coupling. However, with $N_{st} = 2$ and $U_0 = 12\text{ V}$ as shown in figure 3.6b, the peak voltage at the control winding is already higher than about 5 V and the zener diodes prevent higher peak voltages.

The frequency of the oscillation in the simulation is obtained looking at a fourier transform plot. However, it is difficult to predict the inductance of the cornered primary coil and the value obtained in the experiment measuring the frequency and using equation 3.5 cannot be used for the simulation because it is necessary to enter a value for L_2 and L_3 separately. These inductance values are not half of the total primary inductance value because the "two" inductors are coupled and the coupling is unknown. Consequently, the inductance values of L_2 and L_3 need to be altered until the frequency in the simulations equals the one measured in the experiment. The inductance values L_1 and L_2 entered are usually about 1 μH to 4 μH (depending on the coupling factor applied in the simulation and the number of windings), the frequency is about 50 kHz to 150 kHz, however, the values for the final setup are discussed later in this section. With these inductance values, the current I_{pr} observed in the simulation is in accordance to the value obtained by equation 3.7.

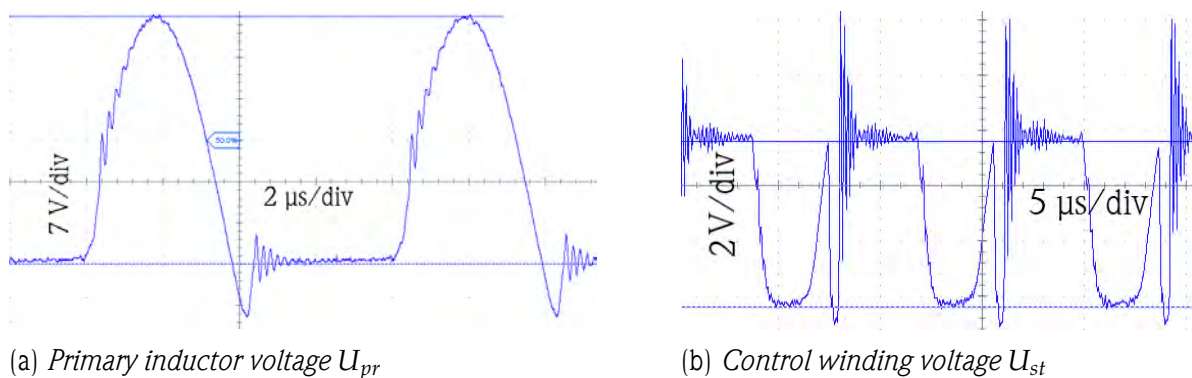


Figure 3.6.
Oscilloscope measurement of voltages in the Royer oscillator for $U_0 = 12\text{ V}$

3.2.2. Dimensioning of the Components

Figure 3.4 shows the electronic schematic including the values chosen for the different components. The constructed induction heating can be seen in figure 3.7.

It is necessary to use fast switching power transistors for this circuit. Many transistors of this category were tested³ that fulfilled the requirements of a maximum collector current around 10 A

³tested transistors: BUT 12A ISC, BUL 58D STM, BUV27, BUV26, BUF 450A ISC, BU 806, BU 406

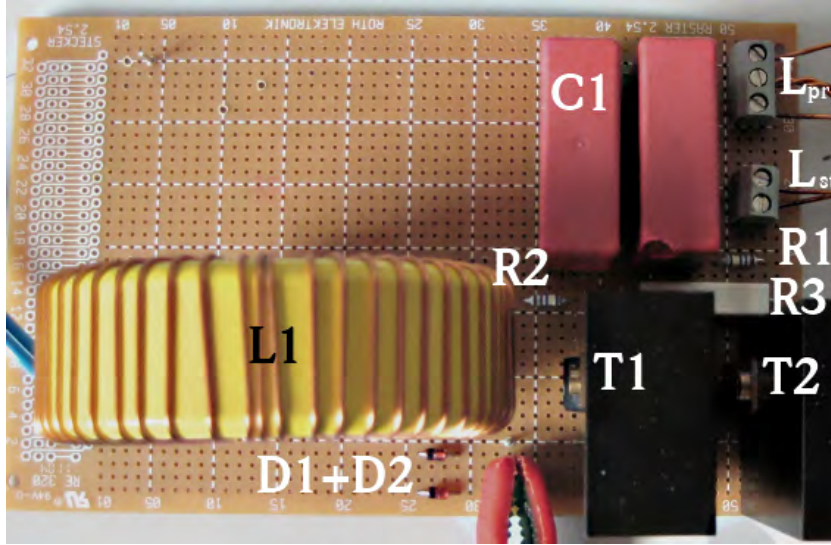


Figure 3.7.
Constructed induction heating

and a maximum collector voltage $> 50\text{ V}$. However, most of them did not work at all, others did not provide a stable signal under load or produced harmonics. The best tested transistor was the BUV27g from ON Semiconductor[®] and is therefore used in the experiment. Unfortunately, there is no LTSpice model for this transistor and therefore the model for the transistor BUV26 is used.

The maximum Emitter-Base-Voltage U_{EBO} for the BUV27 equaling the voltage U_t in the control winding is 7 V [13]. The actual voltage U_{st} depends on the ratio of windings between primary and control inductor N_{pr}/N_{st} . For example, a source voltage of 12 V leads to $U_{pr} \approx 36\text{ V}$ (see eq. 3.6) and consequently a winding ratio $\frac{N_{pr}}{N_{st}} \geq 6$ is required to satisfy the transistor limit. On the other hand, a control inductor with higher number of windings N_{st} provides a better coupling to the primary coil and therefore an undisturbed voltage signal. For that reason, two zener diodes with a breakdown voltage of 5.1 V are used to protect the transistor. This protective circuit was tested in the simulation and the experiment and works reliably. The zener diodes sustain a maximum power of 1.3 W . With the resistance $R_3 = 47\ \Omega$, the protective circuit is able to handle $U_{st} \leq \sqrt{1.3\text{ W} \cdot 47\ \Omega} + 5.1\text{ V} \approx 13\text{ V}$. A higher value of R_3 is not chosen because the Royer oscillator should also work for lower values of U_0 . Nevertheless, the zener diodes diminish the total efficiency very slightly if $U_{st} \geq 5.1\text{ V}$.

The base resistor values $R1$ and $R2$ are determined experimentally observing no-load-current (current output of the voltage source) and the primary coil voltage U_{pr} on the oscilloscope and in the simulation for different base resistor values. For values $> 2\text{ k}\Omega$, the voltage signal is distorted, for values $< 1\text{ k}\Omega$ the no-load-current increases significantly. A value of $1.47\text{ k}\Omega$ is chosen to be optimal.

The choke has to be dimensioned so that the magnetic core does not reach a saturated state under full load current. Otherwise, the permeability μ_r and consequently the inductivity would decrease and directly depend on the magnetic flux density and therefore on the current. This

is undesirable because the choke is needed to block alternating current. According to the simulation, the current through the choke reaches at maximum about 1 A during the transient oscillation at no-load-running and therefore the choke is dimensioned to be able to take 5 A. The full load current in the experiment has been found to be about 1 A as well. The choke works reliably with an inductance higher than 2-3 times the inductivity of the primary coil L_{pr} [12] which is certainly the case for $L1 = 470 \mu\text{F}$.

The magnetic field strength generated by the royer oscillator depends directly on the primary coil current I_{pr} which is, according to equation 3.7, proportional to $\sqrt{C/L}$. Consequently, the number of windings of the primary coil N_{pr} should be chosen as small as possible. However, the coupling between primary and control inductor is worse for small numbers of windings which leads to a disturbed signal. That is why $N_{pr} = 8$ was chosen to get sufficient power and few switching losses. This results in an inductance of about $8 \mu\text{H}$. There were many different winding numbers tested with different coil geometries, especially circled and cornered coils with different dimensions. The final coil geometry is determined by the design of the cooling box described in the previous section. As a consequence of the number of primary windings, $N_{st} = 2$ was chosen to get a high coupling factor. The cross section of the primary coil wire is 1.5 mm^2 . A higher cross section makes it difficult to wind the wire, a lower value leads to more heating of the primary coil. For the control windings, a cross section of 1 mm^2 is sufficient since the current is much lower.

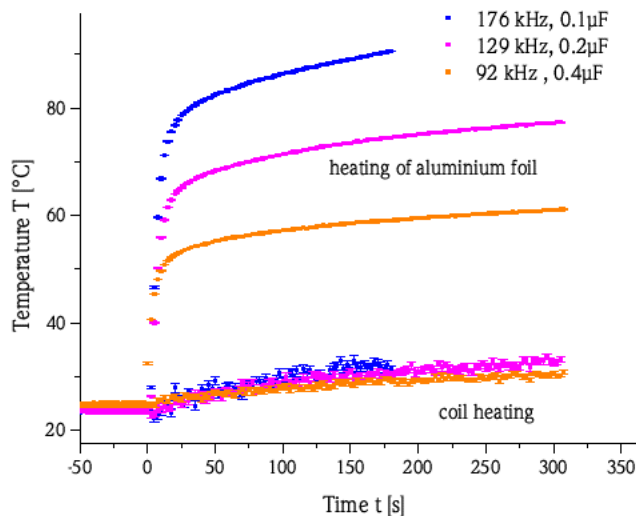


Figure 3.8.
Measurement of heating for different oscillating frequencies

According to equation 3.5, the inductance L_{pr} and the capacity $C1$ determine the frequency of the oscillating circuit. Consequently, it is necessary to find an optimal working frequency to determine the best capacity $C1$. Figure 3.8 shows the result of a measurement performed with all parts of the experimental setup described in this chapter to investigate the dependency of heating on the frequency. This measurement was performed by varying the capacity and adjusting the

3. Experimental Setup

source voltage U_0 to keep the primary coil current I_{pr} determining the magnetic field strength at a constant value of about $I_{pr} = 4.2 \text{ A}$ (see eq. 3.7). As a result of this measurement, it can be seen that the heat input increases with frequency for a constant current I_{pr} . This suggests to use the smallest possible capacity. However, for a smaller capacity, a higher source voltage U_0 is necessary to achieve the same coil current $I_{pr} \propto U_0 \sqrt{C/L}$.

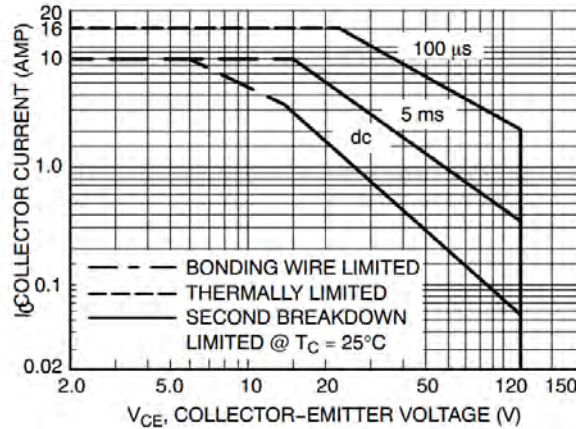


Figure 3.9.

Safe operating area of the transistor BUV27G [13]

The current I_{pr} is limited by the characteristics of the transistors shown in figure 3.9. However, the voltage U_{pr} equaling U_{CE} and the current I_{pr} equaling I_C are not constant, the signal form is a half-wave rectified sine. The average voltage $\overline{U_{CE}}$ equals the source voltage U_0 which is at maximum about 16 V, the average current $\overline{I_C}$ is $U_0 \sqrt{C/L}$. Considering these average values first, for a maximum voltage of 16 V, the current $\overline{I_C}$ must be less than about 4 A. With the calculated inductivity $L_{pr} = 8 \mu\text{H}$ and maximum voltage, this is the case for $C1 \leq 0.5 \mu\text{F}$. However, it is advisable to consider whether the peak current values are within the safe operating area of the transistors as well. For capacities $\leq 0.5 \mu\text{F}$, the frequency is higher than 50 kHz which leads to a peak duration of less than 10 μs . According to the safe operating area shown in figure 3.9, the maximum current is then 16 A. Such a high peak current value is not reached for capacities $\leq 0.5 \mu\text{F}$ since $I_{pr,max} = \pi \cdot 16 \text{ V} \cdot \sqrt{\frac{0.5 \mu\text{F}}{8 \mu\text{H}}} \approx 12.5 \text{ A}$. Consequently, a small capacity of 0.1 μF or 0.2 μF is used to get a high frequency, but if more power is necessary, capacities up to 0.5 μF can be used without problems.

3.3. Readout of Temperature Data

The temperature is measured using pt1000 sensors. The temperature dependence of the pt1000 sensor resistance can be seen in figure 3.10. The green dashed line represents the exact formula for the used sensor type JUMO[®] PCA 1.2010.10L. This sensor type is especially suitable for connections via soft solder connections [14]. The temperature T measured in $^{\circ}\text{C}$ following the

international norm DIN EN 60 751 is [15]:

$$T = \frac{-R_0 \cdot A + \left[(R_0 \cdot A)^2 - 4 \cdot R_0 \cdot B \cdot (R_0 - R) \right]^{\frac{1}{2}}}{2 \cdot R_0 \cdot B} \quad (3.8)$$

R = measured resistance in Ω

$$A = 3.9083 \times 10^{-3} \text{ } ^\circ\text{C}^{-1}$$

$$B = -5.775 \times 10^{-7} \text{ } ^\circ\text{C}^{-2}$$

The resistance R_0 is defined by the resistance value of the sensor type used at $T = 0 \text{ } ^\circ\text{C}$. The corresponding value for a pt1000 sensor is $R_0 = 1 \text{ k}\Omega$. Referring to [15], the complicated formula in equation 3.8 can be linearly approximated in the temperature range between 0 and 100 $^\circ\text{C}$. The approximated formula is

$$T = \frac{R - R_0}{R_0 \cdot \alpha} \quad (3.9)$$

$$\alpha = 3.85 \times 10^{-3} \text{ } ^\circ\text{C}^{-1}$$

and it is represented by the red line. In figure 3.10, it can be seen that there is no considerable

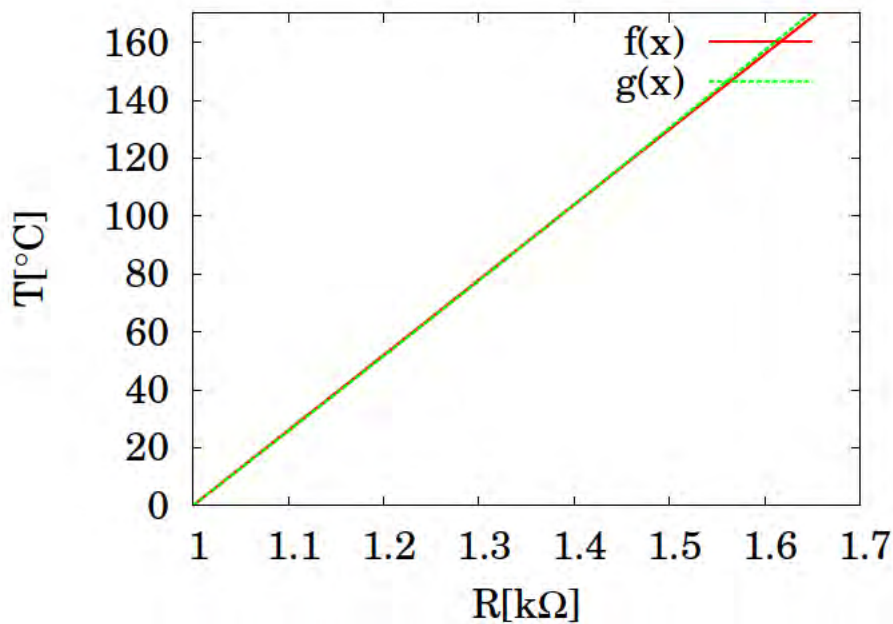


Figure 3.10.

Temperature-resistance curve for the pt1000 sensors; exact formula $g(x)$ (see eq. 3.8) and linear approximation $f(x)$ (see eq. 3.9)

difference between those two formulas in the mentioned temperature range and since the temperatures occurring in the experiment should be within this range as well, the linear form is taken for the temperature readout.

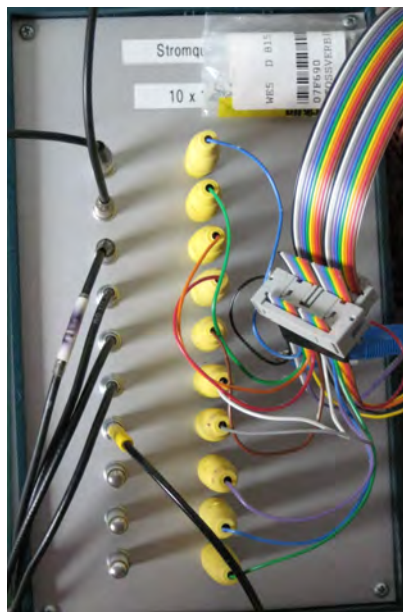
3. Experimental Setup

The temperature dependent resistance of the pt1000 sensors is determined with a current of 1 mA measuring the voltage drop across the sensors (see fig:3.11c). This voltage is measured with a 16 channel ADC of a LogicBox, a universal FPGA-based control and data acquisition system developed at the electronics workshop of the Physikalische Institut Heidelberg. The 16 channels are partitioned in two groups with 8 channels and one ground, respectively. The input voltage range is 0 . . . 2.5 V. According to figure 3.10, the resistance changes about 0.4 k Ω for a temperature change of 100 K. Considering the measurement current of 1 mA, the voltage range for the readout with the LogicBox is about 0.4 V or 4 $\frac{mV}{K}$. This is the maximum sensitivity that could be reached inside the available voltage range of the LogicBox with a simple serial circuit. Using pt1000 sensors with $I = 1$ mA measurement current instead of pt100 sensors with 10 mA has the advantage of less self-heating since the power dissipated is $P = I^2 \cdot R$.

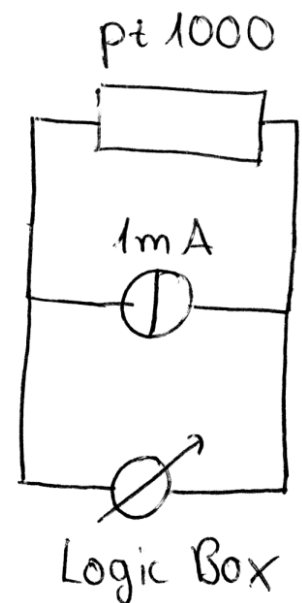
The pt1000 sensors are connected to a 1 mA current source with 10 channels via lemo cables. The voltage is measured parallel to these sensors. Consequently, 10 channels of the 16 channel ADC are connected which is done with a flat ribbon cable and banana jacks. The two different grounds of the logic box (one for channels 0-7, one for 8-15) are connected to the same ground of the current source. Those six channels that are never connected to the current source are grounded via a 50 Ω resistor. Those channels which are plugged to banana jacks but not needed for a certain measurement are all the same connected to the current source, but the missing pt1000 sensors are replaced by 1.2 k Ω resistors. This contact termination minimizes parasitic pickup. Figure 3.11 shows the electrical connections of the LogicBox and the current source.



(a) LogicBox



(b) Current source



(c) Wiring schematic of one channel

Figure 3.11.
Connections for temperature data readout

The LogicBox is connected via USB to a computer. The readout of temperature data is done utilizing LabView[®], the necessary virtual instruments to read out data from the ADC are provided

by the electronics workshop.

First of all, a calibration is necessary to convert the bit number given by the ADC to the measured voltage. This calibration is done for each single channel used for temperature measurements. Figure 3.12 shows the corresponding measurement diagramm for one such calibration. The data points are fitted linearly and the resulting linear equation is used for the temperature readout of the corresponding channel. Furthermore, the actual current of each current source channel was measured. In this way, the resistance of the pt1000 sensor can be calculated from the obtained voltage using Ohm's law. The temperature is then given by equation 3.9.

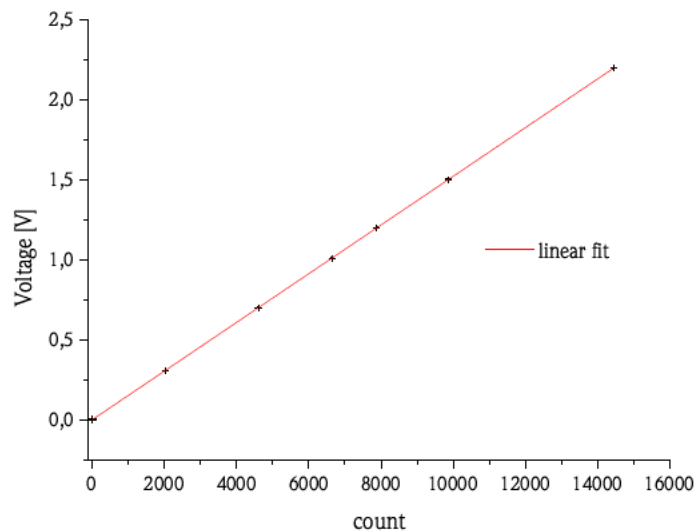


Figure 3.12.
Exemplary calibration of an ADC channel

The LabView programm written for the temperature readout allows to adjust how often the ADC is read out per second. Moreover, results are averaged over an adjustable number of seconds and written into a textfile including their statistic errors. By default, the temperature is measured 100 times per second and averaged over five seconds. This setting is used for most measurements. In addition to that readout into a text file, the temperature trend is monitored online whereby the values taken for this monitoring are always averaged over one second. Furthermore, the elapsed measuring time and the exact temperature value for the last second are displayed on the user interface which can be seen in the appendix as well as the LabView programming (figure A.1 and A.2).

4. Theory and Simulation of Heat Transfer by Forced Convection

It is intended to cool the monolithic active pixel sensors in the Mu3e experiment by forced convection produced by a constant helium gas flow. This chapter describes the cooling process with some principles of thermodynamics and fluid mechanics. To predict the temperature profile of the solid phase as well as of the helium in dependence of the gas volume flow, the basic ideas of fluid dynamics and boundary layer theory are given at first.

In fluid mechanics, in many cases so-called fluid "parcels" are considered. They may be chosen very small, but large enough to achieve an apparently continuous medium so that the molecular composition can be neglected [16]. Due to mass conservation for each considered fluid parcel, a continuity equation is obtained in the form

$$\frac{\partial \rho}{\partial t} + \vec{\nabla} \cdot (\rho \vec{v}) = 0 \quad (4.1)$$

with fluid density ρ and the velocity field

$$\vec{v} = \begin{pmatrix} u \\ v \\ w \end{pmatrix}. \quad (4.2)$$

If an incompressible flow is assumed, so that $\frac{\partial \rho}{\partial t} = 0$, one obtains $\vec{\nabla} \cdot \vec{v} = 0$ and for a two-dimensional problem

$$v \, dx = u \, dy. \quad (4.3)$$

In order to calculate the velocity field \vec{v} , the equation of motion given by the *Navier-Stokes equation* needs to be solved. For incompressible flow and constant dynamic viscosity ν , it takes the form of

$$\frac{d\vec{v}}{dt} = \frac{\partial \vec{v}}{\partial t} + (\vec{v} \cdot \vec{\nabla}) \vec{v} = -\vec{\nabla} \Phi - \frac{1}{\rho} \vec{\nabla} p - 2 (\vec{\Omega} \times \vec{v}) + \nu \Delta \vec{v}. \quad (4.4)$$

Φ = Gravitational field

p = pressure

$\vec{\Omega}$ = Angular speed of Earth's rotation

The Navier-Stokes equation is non-linear which causes chaotic phenomena (turbulence). The *Reynolds number*¹ is an indicator whether turbulent phenomena must be taken into consideration. It is defined by [16]

$$\text{Re} = \frac{\text{Inertial force}}{\text{Frictional force}} = \frac{\left| \left(\vec{v} \cdot \vec{\nabla} \right) \vec{v} \right|}{|\nu \Delta \vec{v}|}. \quad (4.5)$$

If a fluid flows over a solid phase, there is a region called *flow boundary layer* with thickness δ of variable velocity built up between the solid phase and the free fluid stream due to adhesion forces. In analogy to this flow boundary layer, there is a *thermal boundary layer* with thickness δ_t if the solid phase is at a temperature T_w different from that of the free stream, T_∞ [17]. The boundary layer thicknesses δ and δ_t are defined as the distances at which one obtains

$$u(\delta) = 0.99 \cdot u_\infty \quad (4.6)$$

$$T_w - T(\delta_t) = 0.99 (T_w - T_\infty) \quad (4.7)$$

with the horizontal velocity of the free fluid stream u_∞ at temperature T_∞ and the vertical profile of the horizontal velocity component $u(y)$ and of temperature $T(y)$. In general, $\delta \neq \delta_t$ can be derived.

4.1. Laminar Gas Flow over a Flat Solid Surface

As a model of the experimental setup described in chapter 3, a two-dimensional, incompressible and laminar gas flow over a flat solid surface with sharp leading edge is considered. The coordinate system is chosen with x-direction parallel to the surface and y-direction perpendicular to it, the origin of coordinates is at the leading edge of the solid surface. The z-direction is not considered because there are no temperature or velocity gradients expected in this direction (neglecting the spatial limitation of the experimental setup in this direction).

Figure 4.1 shows a sketched boundary layer over a flat surface. The whole grey highlighted part is the area called *boundary layer*, the dashed line shows the boundary limit defined by equation 4.6.

4.1.1. Analytical Description of Heat Transfer

The Reynolds number at length x along the surface for this problem is given by

$$\text{Re}_x = \frac{u_\infty x}{\nu} \quad (4.8)$$

and turbulent phenomena are expected for values larger than $\text{Re}_{x_{\text{critical}}} = 3.5 \cdot 10^5$ [17].

¹named after Osborne Reynolds (1842-1912)

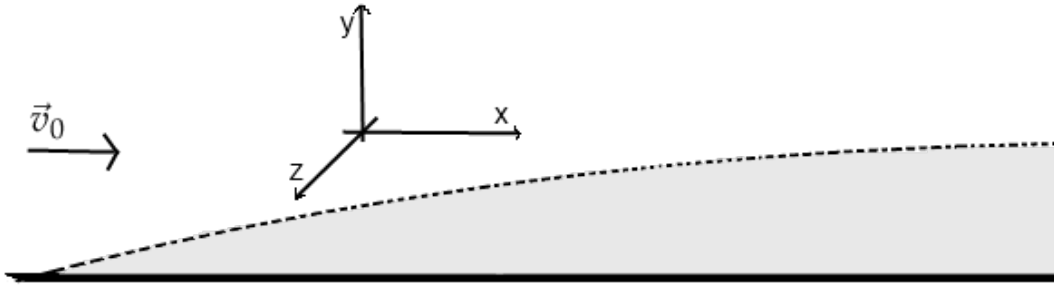


Figure 4.1.
Sketch of the boundary layer over a flat solid surface

The first step needed to evaluate the heat flux from the solid wall to the flowing gas is to develop the flow field inside the flow boundary layer. The equation that needs to be solved is the Navier-Stokes equation given in 4.4. Neglecting Coriolis and Gravitational force and assuming a steady flow ($\frac{\partial \vec{v}}{\partial t} = 0$) yields for two dimensions

$$\left[\begin{pmatrix} u \\ v \end{pmatrix} \cdot \begin{pmatrix} \frac{\partial}{\partial x} \\ \frac{\partial}{\partial y} \end{pmatrix} \right] \begin{pmatrix} u \\ v \end{pmatrix} = -\frac{1}{\rho} \begin{pmatrix} \frac{\partial}{\partial x} \\ \frac{\partial}{\partial y} \end{pmatrix} p + \nu \left[\frac{\partial^2}{\partial x^2} + \frac{\partial^2}{\partial y^2} \right] \begin{pmatrix} u \\ v \end{pmatrix}. \quad (4.9)$$

To simplify this equation, a scale analysis is performed and some so-called *boundary layer approximations* [18] which are valid inside the boundary layer (see figure 4.1) are made:

1. The length scale in x-direction L is long compared to the one in y-direction, δ , so that $\delta \ll L$.
2. Velocity scale in x direction is of order u_∞ , the free stream velocity.
3. $\frac{\partial p}{\partial y} = 0$

The velocity scale in y-direction V can be estimated using the continuity equation in the form of equation 4.3 obtaining $\frac{u_\infty}{L} \approx \frac{V}{\delta}$ and therefore $V \approx \frac{u_\infty \delta}{L}$. With this dimensional analysis, the x-component of equation 4.9 and the order of magnitude of each term inside the boundary layer yield

$$\begin{aligned} u \frac{\partial u}{\partial x} + v \frac{\partial u}{\partial y} &= -\frac{1}{\rho} \frac{\partial p}{\partial x} + \nu \frac{\partial^2 u}{\partial y^2} + \nu \frac{\partial^2 u}{\partial x^2} \\ \frac{u_\infty^2}{L} + \frac{Vu_\infty}{\delta} &\approx \frac{\Delta p_x}{\rho L} + \nu \frac{U}{\delta^2} + \nu \frac{U}{L^2} \end{aligned} \quad (4.10)$$

Regarding $\delta \ll L$, it can be seen that $\nu \frac{\partial^2 u}{\partial x^2} \ll \nu \frac{\partial^2 u}{\partial y^2}$ and so the last term in equation 4.10 can be neglected. The approximation that there is no pressure gradient in y-direction makes the y-component of equation 4.9 redundant [18]. Looking again at the flow past a flat plate, there is no considerable pressure gradient in x-direction and therefore equation 4.9 becomes

$$u \frac{\partial u}{\partial x} + v \frac{\partial u}{\partial y} = \nu \frac{\partial^2 u}{\partial y^2}. \quad (4.11)$$

This is the equation of motion for the the boundary layer of a two-dimensional laminar gas flow past a flat plate. The boundary conditions are:

$$\left. \begin{aligned} u(y=0) &= 0 \\ v(y=0) &= 0 \end{aligned} \right\} \text{"no-slip-condition"} \quad (4.12)$$

$$u(y=\infty) = u_{\infty}$$

The solution of equation 4.11 with the boundary conditions of equation 4.12 must be performed

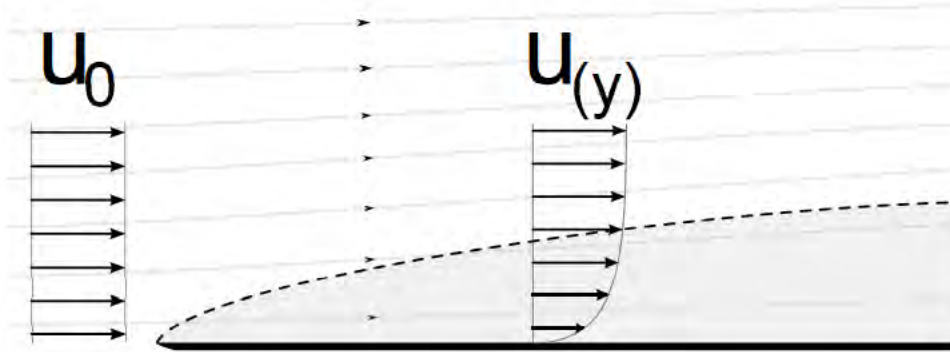


Figure 4.2.

Velocity profile of a laminar boundary layer created by a free gas flow past a flat plate. [19]

numerically ("*Blasius problem*"). Figure 4.2 shows the velocity field, the vertical velocity profile $u(y)$ and the boundary layer of the numerical solution. An important result of this solution is [17]

$$\frac{\delta}{x} = \frac{4.92}{\sqrt{u_{\infty}x/\nu}} = \frac{4.92}{\sqrt{Re_x}} \quad (4.13)$$

As it can be seen in figure 4.2, the boundary layer limit shown by the dashed line is not a streamline. The whole boundary layer is the grey highlighted area.

The next step to evaluate the heat transfer is to evaluate the temperature profile in the thermal boundary layer using the velocity profile derived. It is possible to use *Fouriers law of heat conduction* in differential form at $y = 0$ because of $u(y = 0) = v(y = 0) = 0$ (see eq. 4.12) and therefore no fluid is moving at the wall. [17]

$$q_w = \frac{\partial (Q/A)}{\partial t} \Big|_{y=0} = -k \frac{\partial T}{\partial y} \Big|_{y=0} \quad (4.14)$$

$$Q/A = \text{heat energy per area} \quad \left[\text{J/m}^2 \right]$$

$$k = \text{thermal conductivity of the gas} \quad \left[\text{W/K m} \right]$$

$$q_w = \text{local heat flux at the wall} \quad \left[\text{W/m}^2 \right]$$

Equation 4.14 can be rearranged using the dimensionless *Nusselt number* Nu as the ratio of

convective to conductive heat transfer across the boundary

$$\text{Nu}_x = \frac{hx}{k} = \frac{q_w x}{k(T_w - T_\infty)} \quad (4.15)$$

with the *convective heat transfer coefficient* h . The local heat flux at the wall q_w in equation 4.15 can be replaced using equation 4.14 leading to [17]

$$\text{Nu}_x = - \left(\frac{x}{T_w - T_\infty} \right) \frac{\partial T}{\partial y} \Big|_{y=0} = \frac{\partial \left(\frac{T_w - T}{T_w - T_\infty} \right)}{\partial (y/x)} \Big|_{y=0} \equiv \frac{\partial T'}{\partial (y/x)} \Big|_{y=0} \quad (4.16)$$

with the dimensionless "temperature" profile

$$T' = \frac{T_w - T}{T_w - T_\infty}. \quad (4.17)$$

Equation 4.16 makes it possible to predict the heat flux from the wall to the gas by knowing $\frac{\partial T'}{\partial y}$ at $y = 0$. Therefore it is necessary to predict $T'(x,y)$ inside the thermal boundary layer whilst taking into account the velocity profile that is shown in figure 4.2. For this prediction, it is necessary to make some approximations [17]:

- The thermodynamic properties of the gas are not affected by pressure and density changes, so that k is constant.
- The flow is incompressible, so that equation 4.3 is valid.
- The dynamic viscosity ν is unaffected by temperature changes
- Potential and kinetic energy changes are negligible in comparison to thermal energy changes

That allows us to use the energy equation for a constant pressure flow field [17]:

$$\rho c_p \left(\underbrace{\frac{\partial T}{\partial t}}_{\text{energy storage}} + \underbrace{\vec{u} \cdot \vec{\nabla} T}_{\text{enthalpy convection}} \right) = \underbrace{k \Delta T}_{\text{heat conduction}} + \underbrace{\dot{\rho}_q}_{\text{heat generation}} \quad (4.18)$$

c_p = specific gas heat capacity at constant pressure

ρ_q = heat density

As before in the derivation of the velocity field, we assume a steady state $\frac{\partial T}{\partial t} = 0$. Additionally, there are no heat sources in the flow field and therefore in two dimensions equation 4.18 takes the form

$$u \frac{\partial T}{\partial x} + v \frac{\partial T}{\partial y} = \alpha \left(\frac{\partial^2 T}{\partial x^2} + \frac{\partial^2 T}{\partial y^2} \right) \quad (4.19)$$

with the thermal diffusivity

$$\alpha = \frac{k}{\rho \cdot c_p} \quad \left[\text{m}^2/\text{s} \right] . \quad (4.20)$$

Performing a scale analysis for the boundary layer area in the same way as in equation 4.10 yields $\frac{\partial^2 T}{\partial x^2} \ll \frac{\partial^2 T}{\partial y^2}$ and therefore

$$u \frac{\partial T}{\partial x} + v \frac{\partial T}{\partial y} = \alpha \frac{\partial^2 T}{\partial y^2} . \quad (4.21)$$

Comparing equations 4.21 and 4.11 shows that they are similar apart from the constants α in 4.21 and ν in 4.11. The dimensionless *Prandtl number* is defined as follows: [17]

$$\text{Pr} = \frac{\nu}{\alpha} . \quad (4.22)$$

For simple monoatomic gases counts $\text{Pr} \approx \frac{2}{3}$. For helium at standard conditions, the Prandtl number is 0.664 [20]. The Prandtl number determines the ratio of the thicknesses of thermal and flow boundary layer. From equations 4.21 and 4.11 can be derived that [17]

$$\frac{\delta_t}{\delta} = \text{Pr}^{-\frac{1}{3}} \quad 0.6 \leq \text{Pr} \leq 50 . \quad (4.23)$$

The exact solution of equation 4.21 must be calculated numerically and depends on the boundary conditions. For a constant wall temperature T_w , the solution of equation 4.21, considering the solution of 4.11, is [17]

$$\text{Nu}_x = 0.332 \cdot \text{Re}_x^{\frac{1}{2}} \cdot \text{Pr}^{\frac{1}{3}} \quad \text{Pr} \geq 0.6 \quad (4.24)$$

and for the assumption of a constant heat flux q_w from the solid surface to the fluid [17]

$$\text{Nu}_x = 0.453 \cdot \text{Re}_x^{\frac{1}{2}} \cdot \text{Pr}^{\frac{1}{3}} \quad \text{Pr} \geq 0.6 . \quad (4.25)$$

Since several assumptions and approximations were made to obtain these results, there are some conditions which need to be fulfilled for these calculations to be valid [17]:

- $\text{Re}_L \leq \text{Re}_{L_{\text{critical}}} = 3.5 \cdot 10^5$.
- *Mach number* $\text{Ma} \equiv \frac{u_\infty}{c_s} < 0.3$ with sound speed $c_s = 330 \frac{\text{m}}{\text{s}}$.
- *Eckert number* $\text{Ec} \equiv \frac{u_\infty^2}{c_p} (T_w - T_\infty) \ll 1$ which means that heating by viscous dissipation does not play any role.

As in the following calculations the velocity u_∞ is the variable that needs to be determined, it is necessary to assume that these conditions are fulfilled and to verify this afterwards.

4.1.2. Calculations for the Experimental Setup

In this section, the results of the previous section are applied to the experimental setup described in chapter 3. The length of the flat surface is therefore 8.5 cm. The heated probe is intended to be cooled by helium at room temperature. Consequently, $T_\infty = 20^\circ\text{C}$ is assumed.

First of all, the gas velocity required for a sufficient cooling is calculated for the assumption of a constant wall temperature T_w . This assumption accounts for the good heat conductance of aluminium and silicon which are the specifying materials of the measurement setup. The expected heat output of the pixel sensors is 100 mW/cm^2 and therefore it is attempted to achieve this value with the setup. The highest temperature of the cooled surface should not exceed 60°C , equivalent to $\Delta T_{\max} \equiv (T_w - T_\infty)_{\max} = 40\text{K}$. Since T_∞ is a constant, the temperature difference $(T_w - T_\infty)$ does not change and thus $\Delta T \equiv \Delta T_{\max}$. Plugging in the definition of the Nusselt number (see eq. 4.15) and the Reynolds number (see 4.5) to equation 4.24 yields

$$\begin{aligned} \text{Nu}_x &= \frac{h(x) x}{k} = \frac{q_w(x) \cdot x}{k\Delta T} = 0.332 \sqrt{\frac{u_\infty x}{\nu}} \text{Pr}^{\frac{1}{3}} \\ &\Leftrightarrow q_w(x) = 0.332 \frac{k\Delta T}{x} \text{Re}_x^{\frac{1}{2}} \text{Pr}^{\frac{1}{3}} \end{aligned} \quad (4.26)$$

The heat flux q_w may change with the position x along the surface and is therefore unknown. However, the cooling must compensate the heat output of 100 mW/cm^2 . Consequently, the average heat flux $\overline{q_w}$ from the surface to the gas must take the same value. This average heat flux is obtained by integrating over the length L of the surface and therefore yields

$$\begin{aligned} \overline{q_w} &= \frac{1}{L} \int_0^L q_w(x) dx = \frac{1}{L} \int_0^L 0.332 \sqrt{\frac{u_\infty}{\nu}} \text{Pr}^{\frac{1}{3}} k\Delta T x^{-\frac{1}{2}} dx \\ &= \frac{2}{L} 0.332 \sqrt{\frac{u_\infty}{\nu}} \text{Pr}^{\frac{1}{3}} k\Delta T L^{\frac{1}{2}} = 2 q_w(x = L) \end{aligned} \quad (4.27)$$

As a consequence of that, the gas velocity u_∞ can be obtained by writing equation 4.24 at $x = L$ and replacing $q_w(x = L)$ with $\frac{\overline{q_w}}{2}$:

$$\text{Nu}_L = \frac{q_w(L) \cdot L}{k\Delta T} = \frac{1}{2} \frac{\overline{q_w} \cdot L}{k\Delta T} = 0.332 \text{Re}_L^{\frac{1}{2}} \text{Pr}^{\frac{1}{3}}$$

and therefore

$$u_\infty = \nu L \left[\frac{\overline{q_w}}{0.664 k\Delta T \text{Pr}^{\frac{1}{3}}} \right]^2 \quad (4.28)$$

Similar calculations can be made for the boundary condition of a constant heat flux q_w from solid surface to fluid using equation 4.25. In this case, the temperature difference $(T_w - T_\infty)$ varies along the surface. The maximum temperature difference ΔT_{\max} will appear at the end of the

| Quantity | | Helium | Air |
|-------------------------|--------------------------------|--------|--------|
| heat conductivity k | [W/m K] | 0.156 | 0.0263 |
| Prandtl number Pr | | 0.664 | 0.713 |
| dynamic viscosity ν | [10^{-5} m ² /s] | 1.23 | 1.578 |
| c_p | [J/kg K] | 5193 | 1007 |

Table 4.1.

Some thermophysical properties of helium and air at $T = 300\text{K}$ [20]

| Boundary condition | Helium | Air |
|-----------------------|-----------------------------------|----------------------------------|
| $T_w = \text{const.}$ | 8.0 $\frac{\text{cm}}{\text{s}}$ | 370 $\frac{\text{cm}}{\text{s}}$ |
| $q_w = \text{const.}$ | 17.2 $\frac{\text{cm}}{\text{s}}$ | 795 $\frac{\text{cm}}{\text{s}}$ |

Table 4.2.

Calculated results for the free fluid stream velocity u_∞ for helium and air in the experimental setup ($q = 100 \text{ mW/cm}^2$, $L = 8.5 \text{ cm}$, $\Delta T = 40 \text{ K}$)

sample at $x = 8.5 \text{ cm}$ which can be shown as follows:

$$(T_w - T_\infty)(x) = \Delta T(x) = \frac{q_w x}{\text{Nu}_x k} = \frac{q_w x}{0.453 \text{Re}_x^{\frac{1}{2}} \text{Pr}^{\frac{1}{3}}} \propto \frac{x}{\text{Re}_x^{\frac{1}{2}}} = \frac{x}{\left(\frac{u_\infty x}{\nu}\right)^{\frac{1}{2}}} \propto x^{\frac{1}{2}} \quad (4.29)$$

This maximum temperature difference can be inserted into equation 4.25 at $x = L$ to calculate the gas velocity:

$$u_\infty = \nu L \left[\frac{q_w}{0.453 k \text{Pr}^{\frac{1}{3}} \Delta T_{\max}} \right]^2 \quad (4.30)$$

Table 4.1 shows some thermophysical properties of helium and air that are required to calculate the gas velocity that is necessary for a sufficient cooling according to the boundary conditions set. The corresponding results can be seen in table 4.2. The remarkable difference between the values for air and helium can easily be explained by the difference in the thermal conductivity k and the fact that $u_\infty \propto \frac{1}{k^2}$ (see eq. 4.30).

The flow velocity u_∞ can be plotted for different maximum temperature differences and both boundary conditions discussed. The result can be seen in figure 4.3. The red line shows the result for the boundary condition of a constant heat flux q_w , the blue line the corresponding result for constant wall temperature T_w .

With the calculated results for u_∞ it is possible to determine the maximum boundary thicknesses arising at $x = L$ according to equations 4.13 and 4.23. Moreover it is possible to determine the helium volume gas flow $\dot{V} = A \cdot u_\infty$ actually needed to provide the calculated helium flow velocities in table 4.2 in the experimental setup. The inner dimensions of the box are $(8.5 \times 2.5 \times 5)\text{cm}^3$. The sample is fixed at half-height leading to a cross section for the gas flow

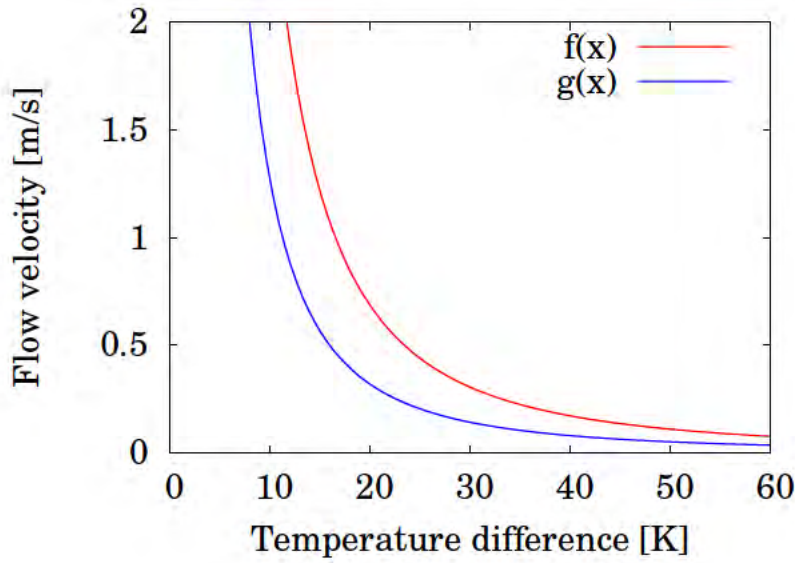


Figure 4.3.

Theoretical prediction on helium flow velocity u_∞ for constant local heat flux q_w ($f(x)$) and constant wall temperature T_w ($g(x)$) ($q = 100 \text{ mW/cm}^2$, $L = 8.5 \text{ cm}$)

| Boundary condition | δ [mm] | δ_t [mm] | \dot{V} [$\frac{\text{L}}{\text{s}}$] |
|-----------------------|---------------|-----------------|---|
| $T_w = \text{const.}$ | 17.8 | 20.4 | 0.05 |
| $q_w = \text{const.}$ | 12.1 | 13.9 | 0.11 |

Table 4.3.

Calculated boundary layer thicknesses at $x = L$ and the corresponding helium volume gas flow for different boundary conditions (calculated for the constraints used for table 4.2)

over the sample of 6.25 cm^2 . This prediction is only a rough estimate on the volume flow, some problems concerning this calculation are discussed in section 5.2.

As shown previously, there are some conditions that need to be fulfilled for the model discussed above to be a good approximation. For helium flow they can be checked with the maximum calculated velocity $u_\infty^{\text{He}} = 0.172 \frac{\text{m}}{\text{s}}$:

$$\begin{aligned}
 \text{Re}_L &= \frac{u_\infty^{\text{He}} L}{\nu} \approx 1.2 \cdot 10^3 \leq 3.5 \cdot 10^5 \quad \checkmark \\
 \text{Ma} &= \frac{u_\infty^{\text{He}}}{c_s} = 5 \cdot 10^{-4} \ll 0.3 \quad \checkmark \\
 \overline{\text{Ec}} &= \frac{(u_\infty^{\text{He}})^2}{c_p} (T_w - T_\infty) \leq 3 \cdot 10^{-4} \ll 1 \quad \checkmark
 \end{aligned} \tag{4.31}$$

4.2. Simulation of Heat Transfer by Forced Convection around 50 μm Silicon Layer

In this section, a Computational Fluid Dynamics (CFD) simulation of heat transfer around a 50 μm silicon layer is described and discussed. A flat surface that is cooled by forced convection as discussed in section 4.1 is not very close to the detector design described in section 2.2, especially because of the fact that most sensors are cooled by forced convection from both sides. To get a more reliable first estimate of the cooling, a CFD simulation is performed using *Autodesk[®] Simulation CFD 2013* which is available in a free version for students and university faculty members. As discussed in section 2.2, the detector consists of thin sensors that are arranged in a polygonal form. One sensor layer consists of 25 μm Kapton[®] foil, 25 μm flex print and 50 μm silicon of the MAPS. The maximum dimensions of a sensor are $36 \times 2\text{cm}^2$. The CFD simulation is performed for one such sensor layer. The geometry and the corresponding coordinates can be seen in figure 4.4.

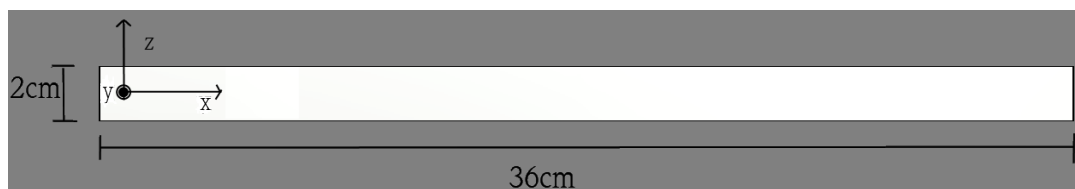


Figure 4.4.
Geometry and coordinate system of the CFD simulation

To perform the simulation, it is necessary to define an outer three-dimensional rectangular box that contains the relevant gas region that encloses the sensor. The dimensions of this outer volume are chosen so that the outer borders do not affect the cooling of the silicon layer. This can be expected to be correct if a homogeneous velocity profile with the initial flow velocity can be observed at the outer region around the silicon layer. Furthermore, boundary conditions need to be defined to generate an external gas flow. At the entry surface, gas temperature and velocity are set. The pressure must not be specified additionally because that would over-constrain the problem for incompressible flow. To define an outlet, the overpressure at the opposite side is set to zero. The remaining boundaries are set to "unknown". According to the software manual, this means that "boundary is open, but no other constraints are applied".

Unfortunately, by adding a 50 μm Kapton[®] film to the silicon layer, energy conservation discrepancies occurred in the simulation. Actually, the power generated inside the silicon did not match the total power flux through the outer surfaces of the sensor. According to the Autodesk support website, the temperature prediction should be unaffected by such discrepancies: [21]

"Autodesk[®] Simulation CFD minimizes the energy equation residual at the nodes, as opposed to forcing fluxes to balance. This helps to ensure an accurate prediction of component temperatures. This often means that the temperature on the object is independent of whether an energy balance is achieved"

The reason for these discrepancies could not be figured out despite the advices given on the support website. For this reason, the simulation is mainly performed with a layer consisting of silicon only. In fact, the differences between the results for the maximum temperature on the sample that are obtained in simulations with Kapton[®] and without are within 1 K. This is reasonable because the heat transport in x-direction is mainly determined by the heat conductance of silicon, which is empirically given by [22]

$$\kappa_{\text{Si}} = \frac{1}{0.03 + 1.56 \cdot 10^{-3} \cdot T + 1.65 \cdot 10^{-6} \cdot T^2} \text{ W/cm K} \quad (4.32)$$

with the temperature T given in K. The CFD simulation software uses a stepwise linear function as an approximation in 200 K steps. Figure 4.5 shows the empirical heat conductivity according to equation 4.32 and the linear approximation of the CFD simulation based on heat conductivity values for $T = -73.15 \text{ }^\circ\text{C}$ and for $T = 126.85 \text{ }^\circ\text{C}$.

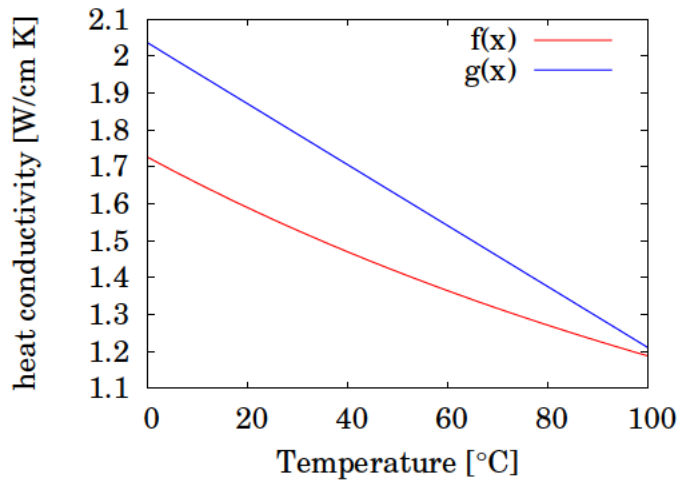


Figure 4.5. Heat conductivity of silicon empirically given ($f(x)$) and linearly approximated by the CFD software ($g(x)$)

The heat conductivity decreases with temperature. At room temperature, an empirical value of about 1.6 W/cm K can be observed, for $T = 100 \text{ }^\circ\text{C}$, a decrease of about 25% to a value of 1.2 W/cm K is obtained. However, for temperatures up to 60 $^\circ\text{C}$, a temperature change of 20 K leads to a lower heat conductivity change than the observed difference between the empirical value and the linear approximation used by the CFD software. A higher heat conductivity is benefiting because it leads to a more balanced temperature profile on the sensor and additionally to a lower maximum temperature.

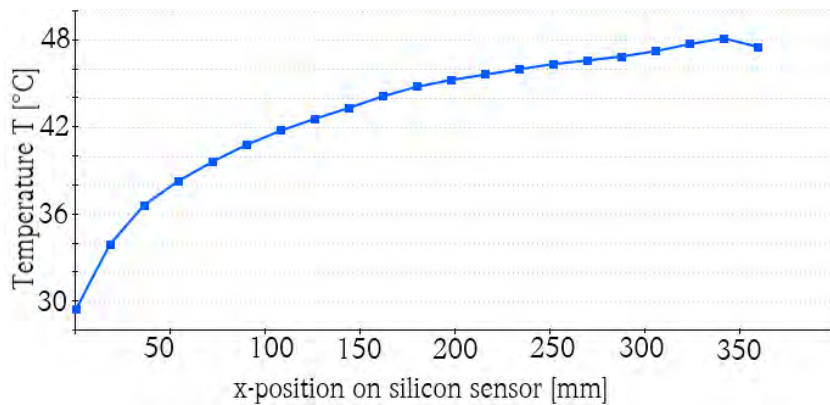
Comparing the heat conductivity of silicon shown in figure 4.5 to that of Kapton[®] which is 0.12 W/m K [8], it can be seen that for all temperatures up to 100 $^\circ\text{C}$, heat is much better conducted in silicon than in Kapton[®]. In spite of this fact, the dimensions in y-direction are much smaller and the kapton film adopts the temperature profile of the silicon quickly. According to section 4.1, the convective heat transfer coefficient h at the boundary does not depend on the heat conductivity of Kapton[®], but on the wall temperature T_w and the heat conductivity k of

4.2. Simulation of Heat Transfer by Forced Convection around 50 μm Silicon Layer

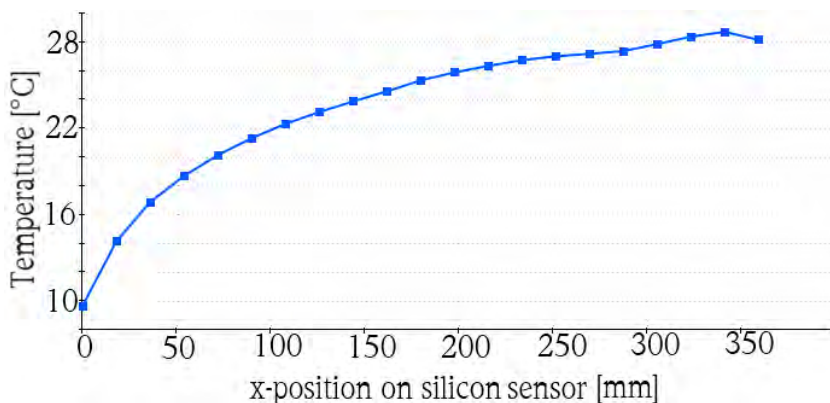
In addition to convective cooling, the simulation considers thermal radiation. It is possible to perform the simulation without radiation, however, the difference is only about 1 K which means that thermal radiation does not help to cool the sensors.

The simulation is performed several times at varying incoming flow speed values u_∞ . For each simulation, vertical and horizontal temperature profiles of silicon and gas are analyzed. Figure 4.6 shows these profiles for a simulation performed with $v = 0.3 \frac{\text{m}}{\text{s}}$. It can be seen that the vertical temperature profile has a similar form as the flow boundary layer shown in figure 4.2.

Additionally, the initial helium temperature T_0 in the simulation is varied. This leads to an almost identical change of the silicon temperature. According to the CFD simulation, the slightly higher heat conductivity for lower temperatures observed in figure 4.5 has therefore no considerable influence on the temperature profile. This can be seen comparing the temperature profiles on the silicon layer for an initial flow velocity of $v = 0.3 \frac{\text{m}}{\text{s}}$ shown in figure 4.7.



(a) Initial helium temperature $T=19.85\text{ }^\circ\text{C}$



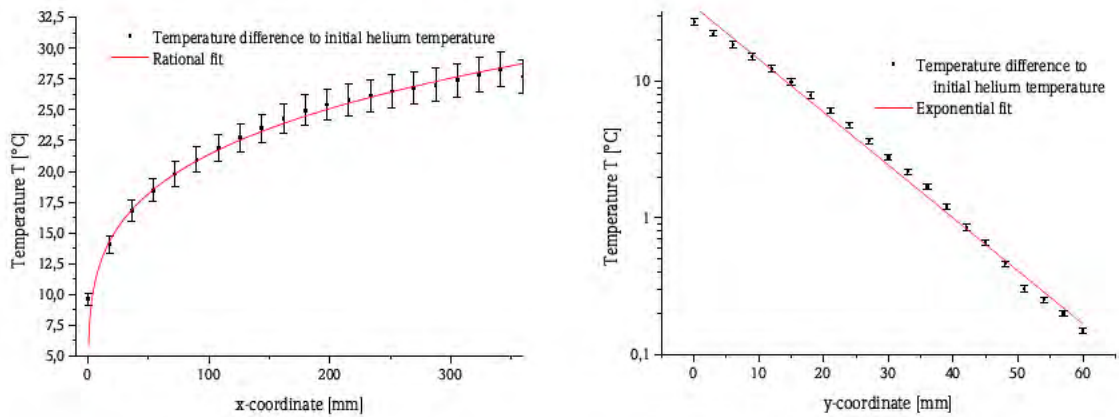
(b) Initial helium temperature $T=0\text{ }^\circ\text{C}$

Figure 4.7.

Temperature profiles on the silicon sensor for different initial helium temperatures

It is therefore reasonable to analyse the difference between the temperatures obtained in the simulation and the initial helium temperature T_0 applied. The following plots do not show the absolute temperature, but the difference ΔT to the initial helium temperature T_0 .

In figures 4.6 and 4.7, it can be seen that the silicon temperature increases in x-direction. This is in accordance with expectations derived in the previous section, in which the temperature profile on the flat surface was calculated for the boundary condition of a constant heat flux q_w in equation 4.29. However, it is not expected that the temperature profile will be proportional to \sqrt{x} because the applied boundary conditions in section 4.1 do not consider finite thermal conduction by the solid material. The thermal conduction of silicon will lead to a more moderate temperature curve than calculated in equation 4.29. Consequently, the temperature difference between the simulated silicon temperature and the applied initial helium temperature is fitted by a function of the form $\Delta T(x) = a \cdot \left(x \frac{1}{\text{mm}}\right)^b$ with free parameters a and b (see figure 4.8a). The error of the temperatures obtained in the simulation is estimated with 5%.



(a) Silicon layer temperature ($y = z = 0$)

(b) Vertical helium temperature ($z = 0, x = 340 \text{ mm}$)

Figure 4.8.

Profiles of temperature differences to initial helium temperature ($19.85 \text{ }^\circ\text{C}$) for a simulation with $v = 0.3 \frac{\text{m}}{\text{s}}$

The vertical helium temperature profile close to the end of the sensor at $x = 340 \text{ mm}$ is shown in figure 4.8b. This temperature curve is fitted exponentially by the form $\Delta T(y) = 10^{(c+d \cdot y)} \text{ K}$ which allows to determine the thermal boundary layer thickness δ_t according to equation 4.7.

The free parameters of the fitted functions in figure 4.8 result in

$$\begin{aligned} a &= 7.3(2) \text{ K} & b &= 0.232(5) \\ c &= 1.55(3) & d &= -0.039(1) \frac{1}{\text{mm}} \end{aligned}$$

The fit parameter b is obtained to be $0.232(5)$ although it was predicted by equation 4.29 to be 0.5 . As discussed previously, this can be explained by the finite heat conduction of silicon leading to a more moderate temperature profile. The $\chi_{\text{red.}}^2$ -value of this fit is about 0.075 .

It can be seen that the exponential fit function does not exactly describe all simulation data points, which results in a $\chi_{\text{red.}}^2$ -value of about 7 . However, the irregularities in the temperature profiles might be solved by a finer mesh for the numeric calculation. The thermal boundary layer

thickness δ_t at $x = 340 \text{ mm}$ can be calculated using the exponential fit in y -direction to solve the condition given in equation 4.7:

$$\begin{aligned} \Delta T(\delta_t) &= 0.01 \cdot \Delta T(y = 0) \\ \Rightarrow d \cdot \delta_t &= \log_{10}(0.01) = -2 \\ \Rightarrow \delta_t &= 51(2) \text{ mm.} \end{aligned} \tag{4.33}$$

By analysing the simulation for different flow speed values, the dependence of the maximum silicon temperature on the initial flow speed u_∞ is investigated. According to equations 4.28 and 4.30, $u_\infty \propto \frac{1}{(\Delta T)_{\max}^2}$ is expected. These equations are calculated for a constant wall temperature T_w or rather a constant local heat flux q_w at the boundary. The condition of a constant wall temperature corresponds to an infinite heat conduction of the solid material whereas a constant heat flux assumes this heat conduction to be zero. Since both equations based on these two different boundary conditions predict the same proportionality between flow speed and maximum wall temperature, this prediction is expected to be correct independent of the finite silicon heat conductivity. However, the simulation is performed considering cooling from both sides of the layer whereas the calculations in section 4.1 consider only cooling over one solid surface. In spite of this fact, it is expected that this influences only the proportionality factor because the surface is doubled and the average local heat flux \bar{q}_w through the boundary is therefore halved. Equation 4.28 predicts $u_\infty \propto \bar{q}_w^2$.

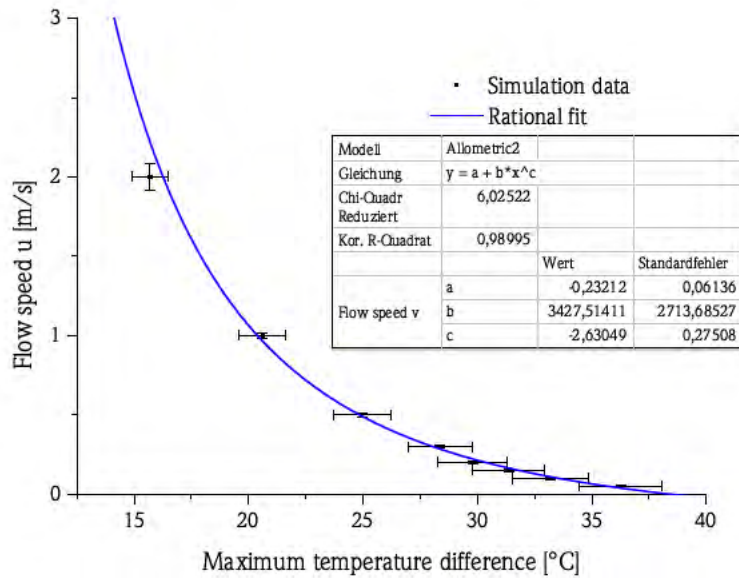


Figure 4.9. Simulated maximum silicon temperature for different initial flow speed values

Figure 4.9 shows the corresponding simulation results. The flow speed error is determined analysing the corresponding velocity profile in x -direction, the temperature error is estimated to be 5%. The blue line represents a rational fit $u_\infty(\Delta T) = a + b \cdot \left(\Delta T \frac{1}{\text{K}}\right)^c$. The results for the

free fit parameters are

$$a = -0.23(7) \frac{\text{m}}{\text{s}} \quad b = 3428(2714) \frac{\text{m}}{\text{s}} \quad c = -2.6(3)$$

The fit function crosses the x-axis already at a temperature difference value less than 40 °C because of the offset parameter a . This is not physically reasonable because a higher temperature difference can be expected without any forced convection. The $\chi_{\text{red.}}^2$ -value of 6.0 shows that the fit does not describe the simulation data satisfactorily, but for a rational fit without offset, an even higher $\chi_{\text{red.}}^2$ -value is obtained. Despite this fact, the difference between the fit value and the theoretical prediction for the exponent is only 2σ .

There are some problems and systematic errors occurring in the simulation that can explain these discrepancies. For smaller velocities, the widening of the helium temperature profiles reaches the boundaries of the outer simulation volume which means that the boundary conditions are no longer well defined. Furthermore, for low gas velocity, a temperature decrease at the very end of the silicon layer is observed and no physical explanation for this phenomena is found. For high flow speed, the boundary layer thicknesses decrease and therefore temperature gradients inside the boundary layer increase. For that reason, a finer mesh would be preferable for higher gas velocities. Finally, more simulation data is required to determine the exact dependence between flow speed and maximum temperature.

In summary, the CFD simulation described in this section allows a first estimate on the cooling effect. For more precise results, the actual detector design should be implemented. This is particularly important because the boundary layer thickness calculated previously for $v = 0.3 \frac{\text{m}}{\text{s}}$ is bigger than the distance between two layers. Therefore, the temperature profile will presumably be influenced. In addition to that, the simulation should be performed with more RAM available to produce more accurate and reliable results.

5. Measurements

5.1. Preparative Measurements

Before quantitative cooling measurements with gas are possible, some preparative measurements are necessary in order to characterize the induction heating and the temperature readout as described in section 3.2 and 3.3.

First of all, the self heating of the pt1000 sensors due to the measurement current of $I_0 = 1 \text{ mA}$ has to be investigated. This self heating can be predicted using a formula given in the sensor datasheet [14] which is

$$\Delta T = I^2 \cdot R_0 \cdot E \quad (5.1)$$

with $R_0 = 1 \text{ k}\Omega$ and a sensor specific self heating coefficient $E = 0.2 \frac{\text{K}}{\text{mW}}$. Consequently, a temperature difference of $\Delta T = 0.2 \text{ K}$ is obtained. The self heating coefficient given in the sensor datasheet is determined for a constant air flow of $0.2 \frac{\text{m}}{\text{s}}$.

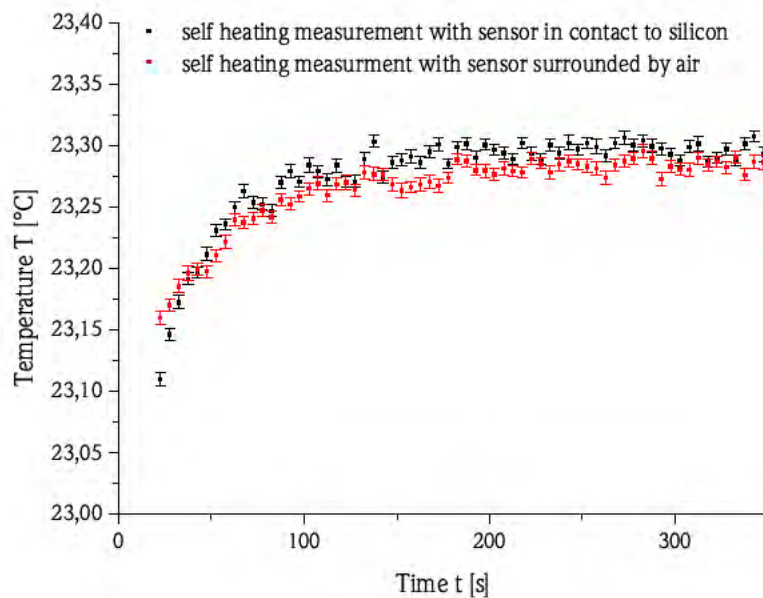


Figure 5.1.
Measurement of self heating without induction heating or gas flow

The measurement to check the self heating is done inside the cooling box described in section 3.1 with one pt1000 sensor that is in direct contact to the silicon layer and with one that measures the gas temperature, in this case the surrounding air. No gas flow is applied and the induction heating is turned off. The gas inlet and outlet are closed to prevent outside influences. The measurement is started and the first results after switching on the measurement current are plotted in figure 5.1. The error bars represent the statistical errors obtained by averaging over 500 voltage measurements within five seconds.

It can be seen that the self heating of both sensors is about 0.2 K. This value is the same as the one calculated with equation 5.1. This is surprising because the self heating coefficient given in the sensor datasheet is determined for a constant air flow and the measurement is done without any gas flow. Furthermore, it is to be mentioned that the observed self heating value of 0.2 K is less than the total measurement error resulting from systematic errors discussed in section 5.3. Additionally, it can be seen in figure 5.1 that the self heating reaches a steady state in less than 200 s and therefore results in a constant offset that could be subtracted from any measurement.

The effect of self heating by the measurement current is indeed dominated by another heating effect resulting from the induction heating. As discussed previously, the pt1000 sensors themselves and their wiring consist of electroconductive material and are therefore heated inductively. This effect is analysed in the following measurement in which the induction heating is turned on, but no sample is inside the box. Consequently, only the pt1000 sensors and other electroconductive setup parts can produce inductive heat. Figure 5.2 shows the result of this measurement for a source voltage of $U_0 = 12\text{ V}$.

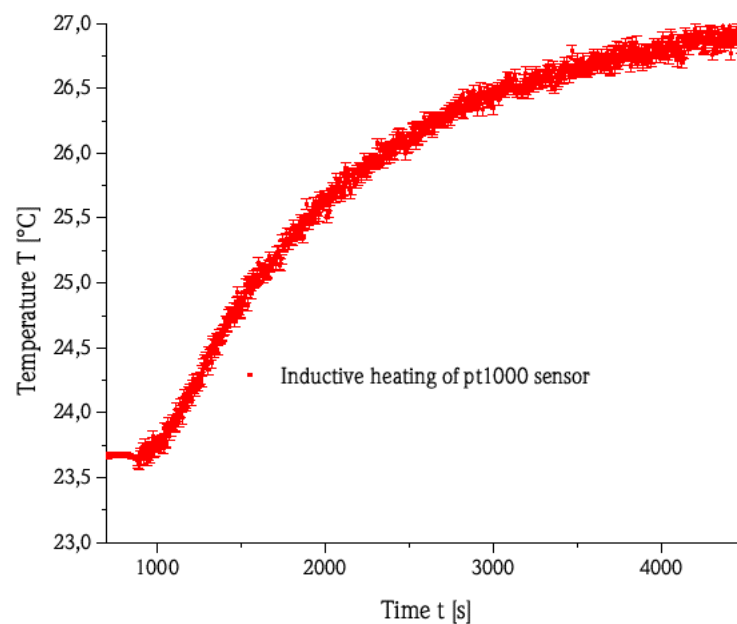


Figure 5.2.
Measurement of temperature increase by inductively produced heat inside the pt1000 sensor

A temperature increase of about 3.5 K can be observed which is certainly no negligible effect. Moreover, the statistical error of the temperature measurement increases if the induction heating is switched on. This effect can be seen by comparing the error bars representing the statistical errors in figures 5.2 and 5.1. This can be explained by the electromagnetic field possibly producing eddy currents inside the sensors and leading to voltage fluctuations. However, the total errors are still smaller than systematic errors discussed in section 5.3.

Furthermore, the delay of the pt1000 sensors measuring temperature changes has to be considered. According to the sensor datasheet, the response time for the sensor type used is [14]

$$\begin{aligned} t_{0.5} &= 7 \text{ s} \\ t_{0.9} &= 22 \text{ s.} \end{aligned} \tag{5.2}$$

The indices indicate the ratio of the temperature difference adapted by the pt1000 sensor to the total temperature change. Both values are determined for a constant air flow of $1 \frac{\text{m}}{\text{s}}$. To verify those values in a measurement, a box is heated to an approximately constant temperature value and afterwards the sensor is brought in. In this measurement, the temperature is averaged over 100 measurements in 1 s, the error bars represent the statistical errors. The result can be seen in figure 5.3.

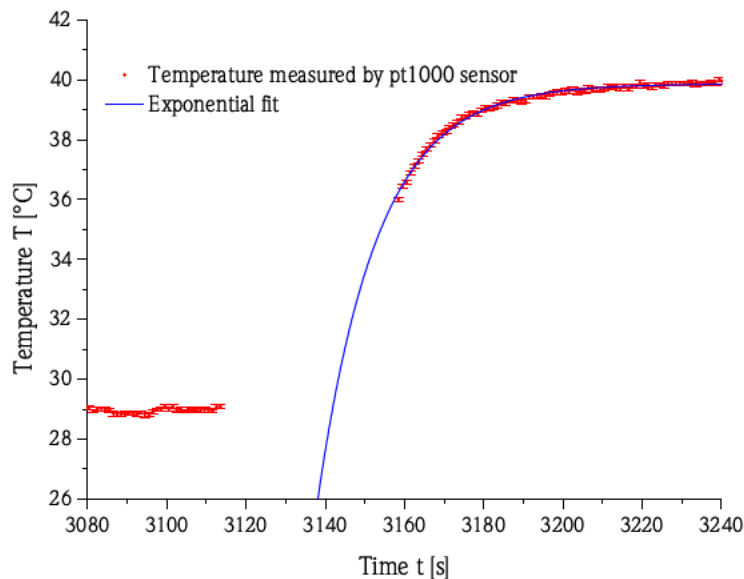


Figure 5.3.
Measurement of temperature sensor response time

Unfortunately, it took some time to bring the pt1000 sensor inside the heated air and no temperature measurement was possible during that time. In spite of this fact, an estimate of the response time can be obtained by the exponential fit curve applied on the measurement data.

The results are

$$\begin{aligned} t_{0.5} &= 10 \text{ s} \\ t_{0.9} &= 30 \text{ s} \end{aligned} \tag{5.3}$$

and the $\chi_{\text{red.}}^2$ -value of the fit is about 1.1.

The results are about 50% higher than the values in the datasheet which is not surprising because the measurement was made without any gas flow. Nevertheless, the results are in the same order of magnitude and allow an estimate of the response time that needs to be considered for the analysis of further temperature measurements.

Beside the temperature readout, the power input in the sample produced by the induction heating needs to be determined. The sensor temperature depends in any case on the heat produced inside it which is therefore an important parameter in every measurement of convective cooling. However, this power input cannot be measured directly. The voltage source connected to the induction heating shows the power input to the induction heating, but power losses need to be considered.

The induction heating is constructed to minimize those power losses. In particular, the harmonic oscillation is always in resonance and the area ratio between the sample surface and the area inside the primary coil is maximized. Nevertheless, there are still some sources of power losses, such as switching losses in the transistors or interference radiation. Since these power losses are unknown and can not be measured directly, the actual power input cannot be determined directly by observing the power output of the voltage source.

The power input is therefore determined considering the temperature gradient $\Delta T/\Delta t$ observed while heating the sample inductively at a certain input voltage U_0 . The input power P is then given by

$$P = m \cdot c \cdot \frac{\Delta T}{\Delta t} \tag{5.4}$$

c = specific heat capacity

m = mass of heated material

Figure 5.4 shows an exemplary measurement in which the temperature gradient is obtained with the previously described method by a linear fit. The temperature curve is only linear at the very beginning of heating because of heat transport to the surrounding air. For some reason, an exponential fit does not describe the temperature curve and therefore a linear fit is made considering about the first 20 s after switching on the induction heating. This results in a temperature gradient of

$$\frac{\Delta T}{\Delta t} = 0.94 \frac{\text{K}}{\text{s}}.$$

The linear fit is done for the temperature curve of all pt1000 that are in direct contact to the silicon surface in the corresponding measurement and the average temperature gradient is determined.

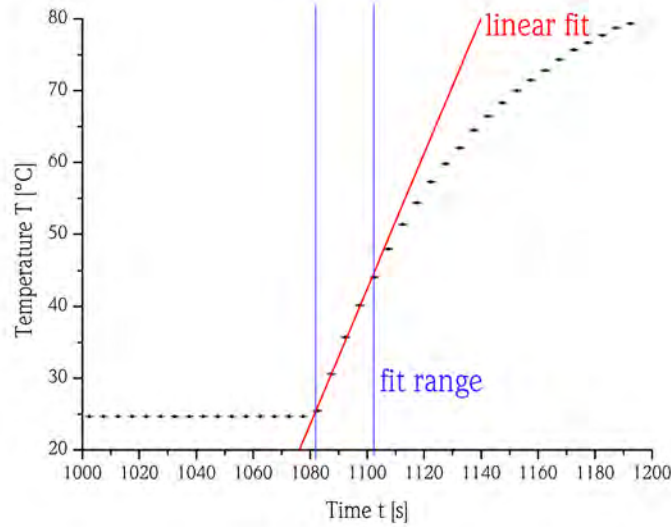


Figure 5.4.
Measurement of heating temperature gradient with $U_0 = 15.5\text{ V}$

For the measurement of which figure 5.4 shows the temperature curve for one of the pt1000 sensors, an average temperature gradient of

$$\frac{\Delta T}{\Delta t} = 0.90(9) \frac{\text{K}}{\text{s}}$$

is obtained. The error could be calculated statistically, however, it is expected that the total error is dominated by systematics because the actual fit value depends strongly on the number of data points considered. Therefore, the error is estimated to be 10%.

The sample heated in this measurement consists of $500\ \mu\text{m}$ thick silicon, $100\ \mu\text{m}$ thick aluminium and $25\ \mu\text{m}$ thick Kapton[®] and measures $8.5 \times 2.5\text{cm}^2$. Table 5.1 shows the properties of silicon, aluminium and Kapton[®] that are used to calculate the sample mass and the input power. The specific heat capacity of silicon is not constant with temperature, but approximated with the value for $T=298\text{ K}$. The Kapton[®] heat capacity does not influence the heat capacity of the sample very much because it is only $25\ \mu\text{m}$ thick and both density and specific heat capacity are smaller than for silicon and aluminium.

| | silicon | aluminium | Kapton [®] |
|--|---------|-----------|---------------------|
| specific heat capacity $\left[\frac{\text{J}}{\text{kg}}\right]$ | 703 | 897 | 109 |
| density $\left[\text{g}/\text{cm}^3\right]$ | 2.33 | 2.71 | 1.42 |

Table 5.1.
Density and specific heat capacity of silicon, aluminium and Kapton[®] [9][8][23]

For the temperature determined previously, this results in a power input of

$$P = 2.1(2) \text{ W}$$

or referred to the sample area

$$q = 99(10) \text{ mW/cm}^2. \quad (5.5)$$

Considering the power output of the voltage source, the efficiency η of the induction heating can be determined. A measurement was done determining the efficiency of the induction heating for different source voltages U_0 . This measurement was done with only aluminium foil of size $2.5 \times 8.5 \text{ cm}^2$. In figure 5.5, showing the corresponding result, it can be seen that the efficiency does not recognisably change for higher source voltages (10 V to 14 V). This fact is very useful because it means that for every sample (the efficiency of the induction heating only depends on the electroconductive material in the sample, so that the silicon and the Kapton[®] should not play any role) and working frequency of the induction heating, only one efficiency measurement for an arbitrary source voltage is necessary. Afterwards, the input power can be determined with the output power of the voltage source multiplied by the efficiency. With the sample used for the cooling measurements described in the following section, an efficiency of $\eta = 0.14(2)$ is obtained.

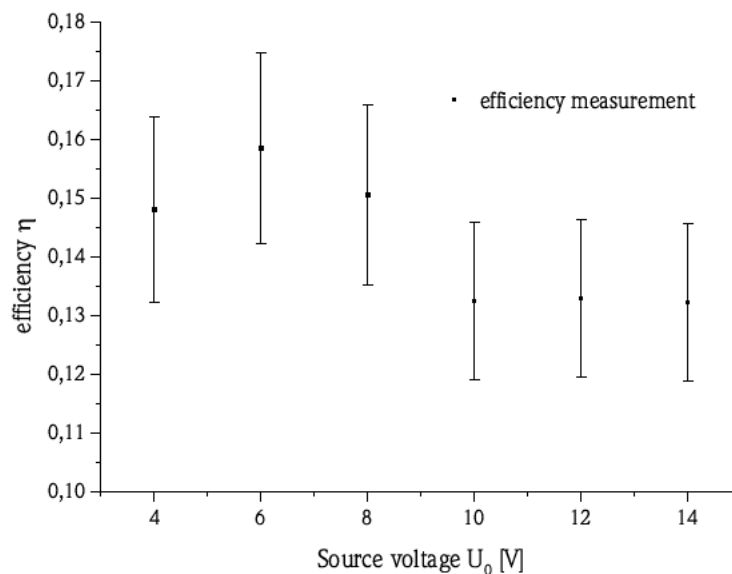


Figure 5.5.
Efficiency of the induction heating

The cooling without forced convection can be analysed by heating a sample and then switching of the induction heating. Figure 5.6 shows the corresponding temperature curve. This measurement was done for a sample consisting of aluminium foil (no Kapton[®] and silicon). The heat capacity is therefore very small and cooling even without forced convection very quick. The

time constants obtained in an exponential fit can therefore not be compared to measurements with additional Kapton[®] and silicon, but they can be attributed to different cooling processes.

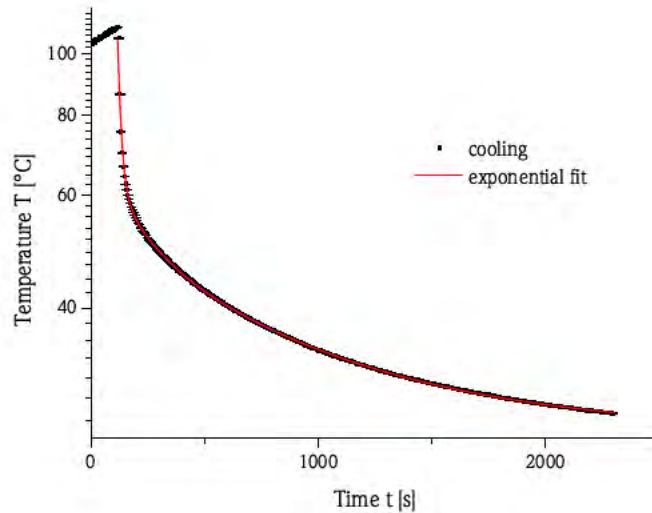


Figure 5.6.
Cooling of aluminium foil inside the cooling box without forced convection

The exponential fit has the form

$$T(x) = y_0 + A_1 \cdot \exp\left(-\frac{x}{t_1}\right) + A_2 \cdot \exp\left(-\frac{x}{t_2}\right) + A_3 \cdot \exp\left(-\frac{x}{t_3}\right) \quad (5.6)$$

and yields the time constants

$$t_1 = 15.9(3) \text{ s} \quad t_2 = 142(3) \text{ s} \quad t_3 = 819(5) \text{ s}$$

and an offset parameter of $y_0 = 25.7(3) \text{ }^\circ\text{C}$. The main cooling processes are heat transfer to the air inside the cooling box, heat transfer to box material due to direct thermal contact and heat transferred from the heated air inside the cooling box through the box walls made of PEEK to the surrounding air at room temperature. Since direct thermal contact between the sample and the box material was minimized (see fig. 3.1a), heat transfer to the air inside the cooling box is expected to be the determining cooling process at the startup of cooling and can probably be assigned to t_1 . The heat exchange between the air inside the box and the surrounding air outside the box at room temperature is expected to be very slow because the box walls are made of PEEK which is a heat-resistant thermoplastic (heat conductivity 0.25 W/m K [9]). This process can therefore be assigned to t_3 . However, the $\chi_{\text{red.}}^2$ -value of about 100 indicates that the fit model used is not complete.

5.2. Cooling Measurements

With the experimental setup described in chapter 3 and the preparative measurements discussed in the previous section, it is possible to investigate the convective cooling with helium. For that purpose, five pt1000 sensors are in contact to the silicon with thermal compound at different positions. Additionally, two pt1000 are positioned to measure the helium temperature.

First of all, the incoming helium temperature is determined. Therefore, the temperature of helium flowing through the box is measured with a pt1000 sensor that has no contact to the silicon. The induction heating is switched off for this measurement. The helium gas cylinder is at room temperature. The expansion of the helium flowing out of the gas cylinder can be considered as an adiabatic process. This expansion is nearly free so that almost no work is done by the system and temperature changes are therefore expected to be small. The measurement results in figure 5.7 show that the helium temperature is about 0.2 K below the measured room temperature. However, this slight temperature decrease might also occur due to cooling of the self heating of the pt1000 sensors discussed previously. Consequently, it is reasonable to assume for the following cooling measurements that the helium is at about room temperature.

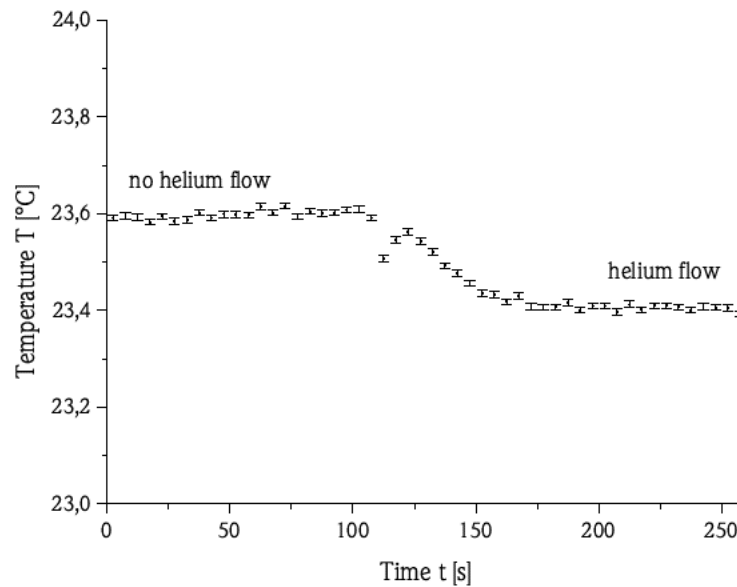


Figure 5.7.

Measurement of helium temperature, $\dot{V} = 0.088 \frac{\text{L}}{\text{s}}$.

Finally, all boundary conditions needed to interpret a cooling measurement are known. The power input can be determined with an efficiency measurement and observing the output power of the source voltage. The helium temperature is known to be about room temperature. In the measurement described in the following, the sample is heated with a source voltage of $U_0 = 15.5 \text{ V}$, which corresponds to the power input value of 99 mW/cm^2 . The room temperature is determined at the beginning of the measurement.

For the following cooling measurement, the power input is held constant and the helium volume flow \dot{V} is varied in a range from $0.021 \frac{\text{L}}{\text{s}}$ to $0.25 \frac{\text{L}}{\text{s}}$. The gas inlet consists of seven holes with a diameter d of 2 mm. The maximum Reynolds number is therefore given by

$$\text{Re}_{\max} = \frac{v_{\max} \cdot d}{\nu} = \frac{4}{7} \frac{\dot{V}_{\max}}{\pi \cdot d \cdot \nu} = \frac{4}{7} \frac{0.25 \frac{\text{L}}{\text{s}}}{\pi \cdot 2 \text{ mm} \cdot 1.23 \times 10^{-5} \text{ m}^2/\text{s}} \approx 1850 \quad (5.7)$$

The transitional Reynolds number for a fully developed flow through a pipe is about 2100 [17]. However, the "pipe" length of the gas inlet is too short to expect a fully developed flow and therefore it is difficult to decide whether laminar flow is achieved or not.

The sample used for this cooling measurement corresponds to the description in chapter 3. It consists of silicon, aluminium and Kapton[®] layered on top of each other and has a size of $8.5 \times 2.5 \text{ cm}^2$. The temperature is measured at five different positions on the silicon surface which allows to analyse the temperature profile of the silicon. Figure 5.8 shows the full temperature curve of all pt1000 sensors used in this measurement. The coordinates indicating the position on the sample refer to the coordinate system used in section 4.2.

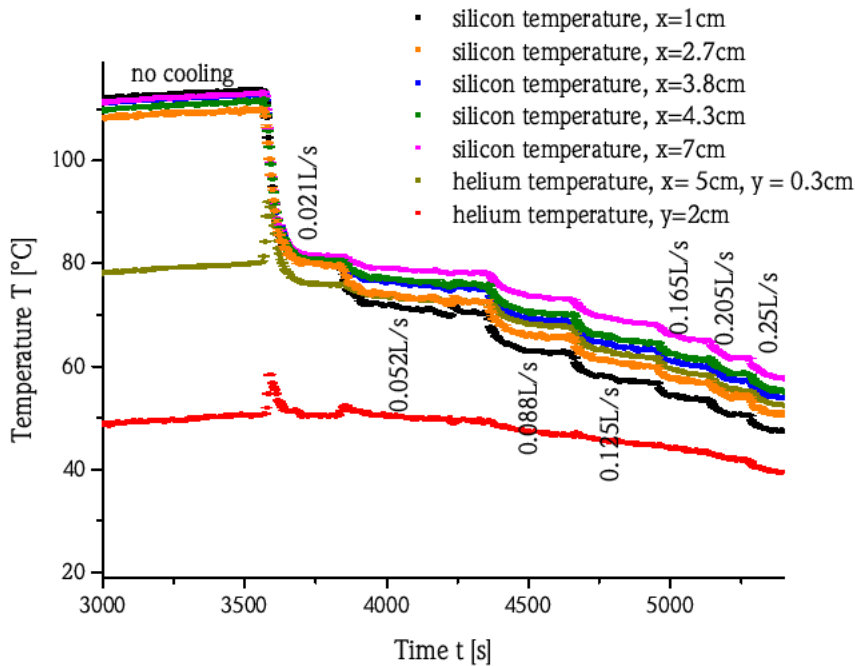


Figure 5.8.

Temperature profile in cooling measurement with sample consisting of Kapton[®], aluminium and silicon of size $2.5 \times 8.5 \text{ cm}^2$ varying helium volume flow.

The temperature profile in figure 5.8 shows that the helium flow cools the sample surface to a lower temperature. Before establishing a helium gas flow, the cooling box is filled with air. After some seconds, a steady state is observed and the temperature remains approximately constant.

5. Measurements

As expected, a higher volume flow corresponding to a higher velocity in x-direction leads to a lower surface temperature.

A short temperature peak is observed with the pt1000 measuring the gas temperatures directly after starting the helium gas flow at about $t=3600$ s. This is probably explainable by the fact that the surface temperature without cooling is considerably higher than in the steady state with applied helium gas flow. This higher temperature is at the beginning flow adapted by the helium at the boundary. After that temperature peak, a steady helium temperature is observed that is lower than the air temperature without any flow. This is reasonable because there was no gas exchange without helium flow. For that reason, the temperature of the helium that is continuously exchanged is lower than the air temperature before although more heat is transported away from the sample.

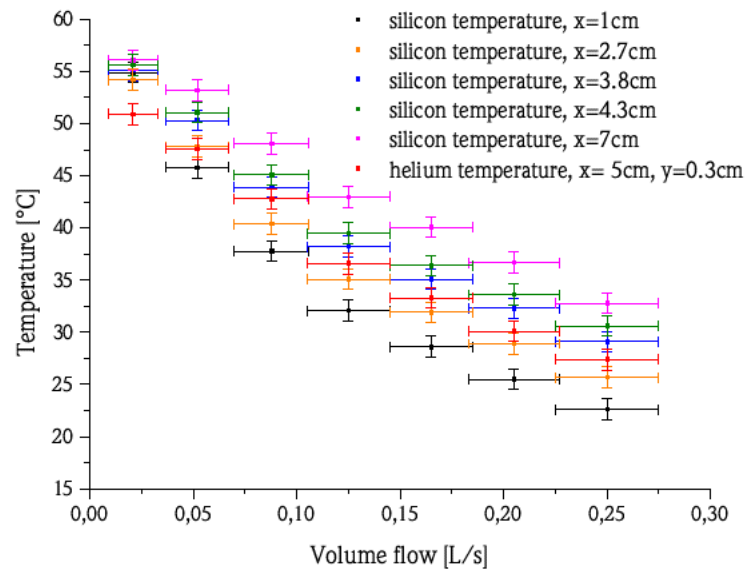


Figure 5.9.

Difference between measured temperature and room temperature for different volume flow values

The temperature that can be observed for different volume flow values is analysed in detail. Therefore, for every pt1000 sensor and for every volume flow adjustment, the temperature profile in this region is fitted exponentially to determine the temperature value in the steady state as the offset value of the exponential fit. Afterwards, the temperature difference ΔT between the measured temperature and room temperature, in this case 25 °C, of every pt1000 sensor besides the one at $y=2$ cm is plotted against the helium volume flow in figure 5.9. The total temperature difference error is estimated with 1 K (see section 5.3).

It would be preferable to plot the temperature against the flow speed along the sample axis because that would allow to compare the results directly to equations 4.28 and 4.30 and to figures 4.3 and 4.9. However, it is not clear how to determine this velocity because it is not

known which cross section is reasonable to use for the calculation. The velocity at the gas inlet is determined by the cross section of the gas inlet which is

$$A_{\text{inlet}} = \frac{7}{4} \pi d^2 \approx 22 \text{ mm}^2. \quad (5.8)$$

Despite this fact, the cross section for the flow through the box is determined by the inner box dimensions which were used for the volume flow calculation in section 4.1.2 and it has a value of 6.25 cm^2 .

The results shown in figure 5.9 can be compared directly to the predictions derived in section 4.1 since the theoretical calculations consider only cooling by forced convection from one side. This condition corresponds to the experimental setup as the gas inlet is positioned about 2 mm above the silicon surface. The sample dimensions fit to the inner dimensions of the cooling box, therefore, there is no gas flow on the other side of the sample. Consequently, only cooling by natural convection (and thermal radiation) is possible on this side. The layout of the gas inlet and the silicon surface can be seen in figure 5.10. Different from that, the CFD simulation considers cooling from both sides. Equation 4.28 predicts $\Delta T \propto \bar{q}_w$ so that a factor of two has to be considered comparing measurement results to simulation results.



Figure 5.10.
Gas outlet, pt1000 sensors and silicon surface layout for cooling measurement

Assuming $\dot{V} \propto u_\infty$ and a constant value of u_∞ in x-direction, $\Delta T \propto \frac{1}{\sqrt{\dot{V}}}$ is expected according to equations 4.30 and 4.28. An increase of the volume flux by a factor of 4 from $0.05 \frac{\text{L}}{\text{s}}$ to $0.2 \frac{\text{L}}{\text{s}}$ is therefore predicted to change the temperature difference by a factor of $\frac{1}{2}$. Comparing this prediction to the results shown in figure 5.9 at $x=7 \text{ cm}$, temperature difference values of about $\Delta T = 53.2 \text{ K}$ ($\dot{V} = 0.052 \frac{\text{L}}{\text{s}}$) and $\Delta T = 36.7 \text{ K}$ ($\dot{V} = 0.205 \frac{\text{L}}{\text{s}}$) are measured corresponding to a temperature decrease by a factor of about $\frac{7}{10}$. Consequently, the temperature changes measured are smaller than predicted. This might be explained by the fact that the free fluid stream velocity is not well-defined in the experimental setup. Different from the predictions based on theoretical calculations and the CFD simulation, the temperature curve for $x = 7 \text{ cm}$ in figure 5.9 looks approximately linear.

The absolute temperature difference values are compared to the theoretical predictions in section 4.1 and the CFD simulation. At the position of $x = 7 \text{ cm}$ on the silicon layer, it seems to be reasonable to consider the cross section of the inner box dimensions of about 6.25 cm^2 to calculate the flow speed in x-direction. Therefore, a volume flow of $0.165 \frac{\text{L}}{\text{s}}$ corresponds to a

5. Measurements

flow velocity of about $26.4 \frac{\text{cm}}{\text{s}}$. The measured temperature difference for this volume flow at $x = 7 \text{ cm}$ is about 40 K (see fig. 5.9).

To compare the measurement values at $x = 7 \text{ cm}$ with the theoretical predictions of section 4.1, equations 4.30 and 4.28 are rearranged to calculate the temperature difference $\Delta T = (T_w - T_\infty)$ at $x=7 \text{ cm}$. The results are given in table 5.2.

| Boundary condition | $\Delta T(x = 7 \text{ cm})$ |
|--------------------|------------------------------|
| q_w constant | 29.0 K |
| T_w constant | 19.8 K |

Table 5.2.

Theoretical temperature difference predictions
($x = 7 \text{ cm}$, $v = 0.25 \frac{\text{m}}{\text{s}}$, $q_w = 99 \text{ mW/cm}^2$)

Both values are considerably smaller than the measured value of about 40 K ($\dot{V} = 0.165 \frac{\text{L}}{\text{s}} \hat{=} u_\infty = 26.4 \frac{\text{cm}}{\text{s}}$) which means that the theoretical calculations predict a better cooling than it was measured in this cooling measurement.

In the CFD simulation, the maximum temperature difference observed was less than 40°C even for very small flow velocities and a sensor length of 36 cm. Figure 4.8a shows the temperature differences observed in the CFD simulation for an initial velocity of $30 \frac{\text{cm}}{\text{s}}$. It can be seen that the temperature difference between silicon temperature and initial helium temperature at $x = 7 \text{ cm}$ is about 19°C . However, the simulation considers cooling from both sides whereas in the measurement, the sample is only cooled on one side. Consequently, both values are in accordance considering a factor of two due to the different surface areas at which cooling by forced convection is considered. For a reliable comparison of absolute temperature values in measurement and simulation, the measurement results need to be reproduced in further measurements and compared to the simulation for different flow speed values and positions on the silicon surface.

In addition to the dependence between temperature and helium volume flow, the temperature profile on the silicon layer itself is investigated and can be seen in figure 5.11. The temperature on the silicon increases in x-direction which is in accordance to the theoretical predictions and the CFD simulation. The temperature difference curves are fitted by a function of the form $T(x) = a + b \cdot x^c$. Equation 4.29 predicts an exponent c of 0.5. In the simulation, an exponent of 0.23 was obtained. However, an even lower exponent is expected in the measurement. The thermal conduction in x-direction in the sample is determined by the thermal conductivity of aluminium which is higher than that of silicon considered in the simulation. Consequently, a more balanced silicon temperature profile is expected as the dimensions in y-direction are much smaller and the silicon is expected to adapt to the aluminium temperature. The free fit parameter c determined in those fits varies in a range from 0.4 to 0.6 and therefore not in accordance to this prediction. However, the χ_{max}^2 -values determined by these fits are larger than 2 for every fit. This leads to the assumption that there must be some systematical errors influencing this temperature measurement.

In figure 5.8, it can be seen that without any helium gas flow, the pt1000 sensors in thermal contact to the silicon do not measure a unique temperature. The temperature values vary by about

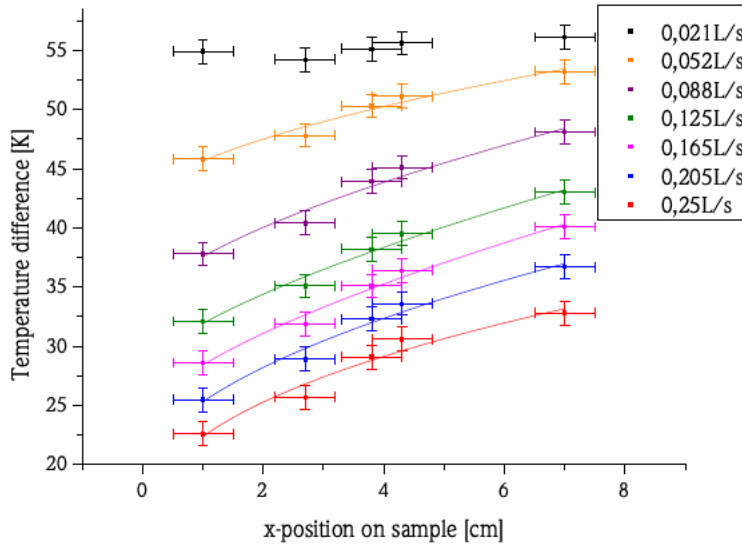


Figure 5.11.

Difference between measured silicon temperature and room temperature for different helium flow and position on the sample. Measurement values are the same as in figure 5.9.

5 K. This could be explained by the fact that the induction heating heats the sample especially in outer regions. Nevertheless, the positions of the pt1000 and the measured temperatures are not in accordance to this explanation. Consequently, the effect seems to be a systematic error based on the thermal contact of the pt1000 sensors to the silicon. It can be expected that this systematic error will influence the measured temperature profile on the silicon layer that can be seen in figure 5.11 and therefore an improvement for further measurements would be important to get a more reliable temperature profile so that it could be compared to theoretical predictions.

A further cooling measurement was performed to investigate the temperature dependence on the power input. For that purpose, the helium volume flow is kept at a constant value of $\dot{V} = 0.088(18) \frac{\text{L}}{\text{s}}$ and the source voltage for the induction heating is varied in a range of 6 V to 16 V. To observe the temperature of the flowing out gas, another pt1000 sensor was installed in front of the gas outlet.

Figure 5.12 shows the corresponding measurement results. The helium temperature at $x = 8.3$ cm is lower than that at $x = 5$ cm. The reason for this effect is the mixing of the gas in front of the outlet leading to a lower average temperature that is measured by the pt1000 directly in front of the gas outlet. With this measured average helium temperature at the gas outlet, it is possible to compare the input power in the silicon with the input power in the helium. In a steady state, both values should be the same. The power input in the helium can be determined rearranging equation 5.5:

$$\begin{aligned}
 P &= m \cdot c \cdot \frac{\Delta T}{\Delta t} \\
 &= \rho \cdot \dot{V} \cdot c \cdot \Delta T
 \end{aligned}
 \tag{5.9}$$

5. Measurements

ρ = helium density

c = specific heat capacity of helium

ΔT = Temperature difference of helium temperatures at gas inlet and outlet

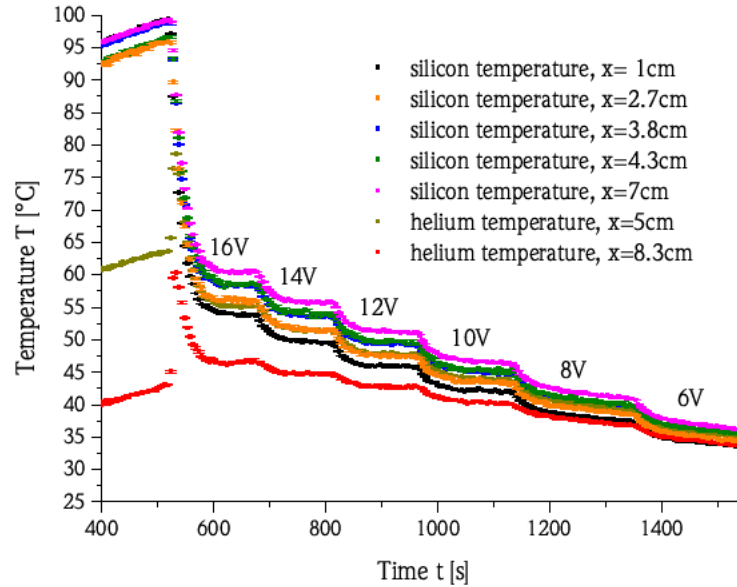


Figure 5.12.

Temperature profile in cooling measurement varying power input

As well as in the previous cooling measurement, the silicon and helium temperatures are obtained using an exponential fit. The room temperature used as an approximation for the helium temperature at the gas inlet was measured to be 25 °C. The power input in the silicon is determined with the output power of the voltage source and the induction heating efficiency of $\eta = 0.14(2)$. In table 5.3, the resulting power values are compared. It can be seen that the measured helium temperatures at the gas outlet are reasonable, but the power input in the helium is calculated too high for low power input and too low for high power input. This might be explained by the fact that heat might be transferred from the helium to the box made of PEEK. However, the power input in the helium should not exceed the power input in the silicon.

Furthermore, the measured temperatures of the pt1000 sensors in dependence of the power input in the sample is analysed. As in the previous measurement, temperature differences to room temperature are considered and shown in figure 5.13. Equation 4.28 predicts for the silicon temperature $\Delta T \propto \bar{q}_w$ for constant flow velocity which is in accordance to the temperature curves observed and shown in figure 5.13.

However, comparing the temperature difference values for $q \approx 100 \text{ mW/cm}^2$ and $\dot{V} = 0.088 \frac{\text{L}}{\text{s}}$ in this measurement with values measured in the previous cooling measurement with varying flow, it can be seen that the values are not the same (see figures 5.9 and 5.13). If both measurements were reproducible, no considerable differences between the measured temperatures

| Source Voltage U_0 [V] | silicon power input [W] | helium power input [W] |
|--------------------------|-------------------------|------------------------|
| 16 | 2.12(32) | 1.73(35) |
| 14 | 1.63(25) | 1.61(34) |
| 12 | 1.24(20) | 1.44(30) |
| 10 | 0.88(14) | 1.24(27) |
| 8 | 0.53(9) | 0.94(20) |
| 6 | 0.23(6) | 0.66(15) |

Table 5.3.

Helium and silicon power input

would be expected because the conditions under which these measurements were performed are nearly the same. The observed temperature values differ from each other by about 10 K to 15 K depending on the sensor position. Comparing figures 5.12 and 5.8, it can be seen that at the beginning of the first cooling measurement, the sample was heated to a higher temperature with no cooling than in the second one. Theoretically, this should not influence the temperatures observed in a steady state after applying a constant helium gas flow. Consequently, this problem needs to be figured out in further measurements so that the absolute temperature values can be interpreted.

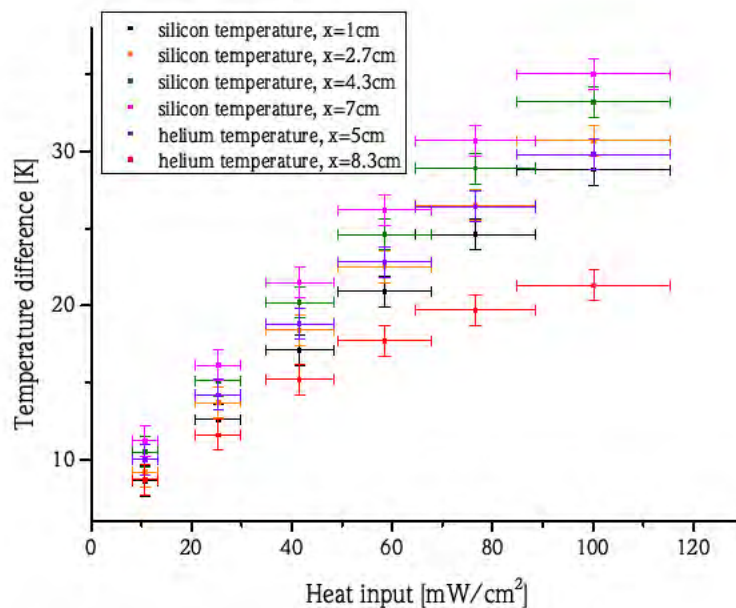


Figure 5.13.

Difference between measured temperature and room temperature for different power input values

5.3. Discussion of Systematic Errors

In this section, systematic errors of the cooling measurements are discussed in more detail. Some problems have already been mentioned in the previous section, such as the thermal contact between the sensors and the sample, and are therefore not reconsidered in this section.

First of all, some systematic errors result from the temperature readout. The used pt1000 sensors themselves have an accuracy of ± 0.3 K [14]. They are connected to the current source via silver wire and lemo cables and plugs. Consequently, the measured resistance includes the resistance of the connectors leading to a temperature offset. However, the resistance of 5 cm silver wire with 0.5 mm diameter is about 1 m Ω and therefore negligible (see fig. 3.10). Moreover, if temperature differences are considered, a constant offset value does not change the result. Another systematic error results from the current source that provides $I = 1$ mA. The exact current value of every channel was determined by measuring the voltage drop over a resistance of 1 k Ω (1% accuracy) so that the exact current value is considered in the LabView temperature readout programming. However, a current error of 1-5% would lead to the same temperature error. In addition to that, other parasitic errors such as cross talk between different input channels to the LogicBox result in an error up to 0.4 K. This can be observed by measuring the same temperature with different pt1000 sensors and observing slightly different results. Temperatures over about 100 °C can not be measured precisely since the linear formula for the pt1000 temperature dependence is not valid in this range.

Beside the temperature readout, the experimental setup is another error source. The thermal contact between the sample and the surrounding materials is minimized, but not completely eliminated. Other effects concerning thermal conduction such as heat transferred from the helium gas to the walls made of PEEK can not be excluded and might influence measurement results. Additionally, other heat sources such as electroconductive material inductively heated or the primary coil of the induction heating may influence the results. To exclude this systematic, a measurement corresponding to the one shown in figure 5.2 would be necessary for every induction heating adjustment and subtracted from the final measurement results. The lemo plugs at the wall of the cooling box should not be touched during a measurement because the transferred heat can be observed with the pt1000 sensors.

Finally, the total error, including statistical errors resulting from averaging over many single measurements, is estimated to be about 1 K for temperature differences. This estimation considers systematic errors occurring in the temperature readout but does not take into account systematics concerning the experimental setup itself.

The helium volume flux is, as described in chapter 3, measured by a rotameter. The position of the float must be measured visually and the flux needs to be adjusted if unintended changes are observed. The error of this measurement is estimated to be about 0.5 scale divisions. Another problem concerning the helium flow are possibly arising turbulences that are difficult to observe and prevent.

6. Discussion and Outlook

The Mu3e experiment aims to detect and to identify the decay $\mu^+ \rightarrow e^+ e^+ e^-$. This decay is lepton flavour violating and therefore suppressed in the (extended) standard model with a branching ratio of $\text{BR}(\mu^+ \rightarrow e^+ e^+ e^-) \approx 1 \times 10^{-50}$. It is intended to measure a branching ratio of $\text{BR}(\mu^+ \rightarrow e^+ e^+ e^-) < 1 \times 10^{-16}$ at 90% confidence level. According to some theories beyond the standard model, this sensitivity allows to detect the decay $\mu^+ \rightarrow e^+ e^+ e^-$ and therefore to indicate the existence of new physics [1].

In order to reach the mentioned sensitivity goal, high-voltage monolithic active pixel sensors (HV-MAPS) thinned to 50 μm are used. They are supported by a Kapton[®] framework and arranged in a polygonal form. This setup is chosen to achieve a high granularity and a low material budget helping to minimize multiple scattering. Cooling of the MAPS sensors is necessary and intended to be achieved by forced convection with gaseous helium.

The cooling of the Mu3e-detector with helium gas needs to be investigated. For that reason, a new experimental setup was designed and constructed that allows to perform measurements on the cooling effect. It consists of an induction heating simulating the heat produced by the pixel sensors. An induction heating is chosen because it allows a contactless power transmission. The sample which is heated by the induction heating consists of Kapton[®], silicon and aluminium. An electroconductive material is required for the induction heating. The other materials and the dimensions ($2.5 \times 8.5 \text{ cm}^2$) are chosen so that they fit to the detector design. The thin sensor layers have a very low heat capacity illustrating the need of contactless power transmission.

The helium gas flow is provided by a special rectangular box designed for these cooling measurements. It allows a sufficient power transmission to the sample by maximizing the ratio between the sample surface and the area inside the primary coil of the induction heating. Direct contact of the sample to surrounding material is minimized in order to reduce thermal conduction.

Moreover, lemo connectors allow the temperature readout with pt1000 sensors. They are connected to a 1 mA current source, the readout is done with a 16-channel ADC of a LogicBox developed at the electronics workshop of the institute. The programming is performed using LabView[®]. The pt1000 sensors can be positioned on the silicon surface or inside the helium gas flow.

The characteristics of the experimental setup were examined in some preparative measurements. It was shown that the self-heating of the pt1000 sensors is about 0.2 K and therefore considerably lower than other systematic effects (see section 5.3). The induction heating without any sample to heat produces a temperature increase measured by the pt1000 sensors of about 3.5 K after about one hour, caused by electroconductive parts in the experimental setup. The power input in the sample was determined considering the temperature gradient at the startup of heating

process. According to these measurements, the power input generated by the induction heating was successfully adjusted to fit to the expected power input in the pixel sensors of about 100 mW/cm^2 . Even more power is possible by increasing the capacity used in the LC-circuit as the main component of the induction heating.

The achieved efficiency of heating a sample containing aluminium as electroconductive material is about 14%. Additionally, the efficiency might be increased by replacing the aluminium foil by iron foil or any other ferromagnetic material.

First measurements were performed with this experimental setup in order to investigate the cooling with helium gas flow. The experimental setup looks promising for a systematical investigation of cooling by forced convection. However, some problems need to be addressed to get more reliable measurement results, concerning particularly absolute temperature values. In the measurements that were performed yet, the absolute temperature values seem to depend on the thermal contact between sensor and sample and on the sample temperature before the helium gas flow is started. Another problem is the prediction of the flow speed. The flow speed can not be measured directly and has to be calculated using a volume flow measurement, but the geometric cross section of the gas flow is not well defined. The helium temperature measured in front of the gas outlet fairly fits to the volume flow and the heat produced in the sample.

Despite the mentioned problems, some conclusions based on the first measurement results are possible. It is shown that the temperature on the silicon sensor increases along the main axis (see fig. 5.11) and that the silicon temperature is approximately proportional to the power input (see fig. 5.13). These results are in accordance with theoretical predictions based on fluid dynamical calculations. However, there are differences between theory and experiment concerning absolute temperature values and concerning the dependence of temperature on flow speed. The reasons for these discrepancies must be figured out in further measurements. Additional measurements could be done using a thermal imaging camera. This measurement could be used to investigate the temperature distributions inside the cooling box qualitatively. Performing quantitative measurements is difficult because of the high reflectivity of silicon surfaces.

In addition to that, it was intended to make comparison measurements with nitrogen or air. Unfortunately, this was not possible yet because of connection problems. These measurements are desirable to investigate the differences in cooling with helium and nitrogen and to compare them to the theoretical predictions.

The measurements and the theoretical predictions based on fluid dynamics are complemented by a CFD simulation. It simulates a gas flow around a silicon sensor layer with dimensions $36 \text{ cm} \times 2 \text{ cm} \times 50 \text{ }\mu\text{m}$. This corresponds to the maximum dimensions in the detector. The simulation results are mainly in accordance with the theoretical predictions and differences explainable by different boundary conditions. The simulation shows that a change of helium temperature leads within errors to an identical change of sensor temperature. A difference between the silicon temperature at the end of the sensor and the helium temperature of about $25 \text{ }^\circ\text{C}$ is predicted for a flow speed of $0.5 \frac{\text{m}}{\text{s}}$ (see fig. 4.9). Unfortunately, some problems mainly attributable to a lack of computer performance impair the precision of the simulation results. A simulation including the actual detector design has to be done in order to get more reliable results.

In the Mu3e detector, pixel sensors need to be cooled. The heat dissipation of this pixel sensors and the maximum temperature that needs to be satisfied are determined by the final pixel chip design and the temperature dependence of pixel sensor characteristics such as the signal-to-noise-ratio. According to these constraints, the helium flow velocity and the corresponding volume flow need to be adjusted afterwards. First measurement results show that a temperature difference between sensor temperature and helium temperature of 32 K and a heat output of 100 mW/cm^2 require a flow velocity of $40 \frac{\text{cm}}{\text{s}}$ (corresponding to a volume flow of $0.25 \frac{\text{l}}{\text{s}}$ in the experimental setup, see fig. 5.9) for a sensor length of 8.5 cm. Further measurements are necessary to confirm the results obtained yet. Reliable measurement results could be used to verify and complement results of a cooling simulation including the actual detector design.

Finally, the experimental setup developed for this thesis and the first measurements together with some theoretical calculations and CFD results provide the basis for a further detailed analysis of the cooling for the Mu3e-detector.

Bibliography

- [1] A. Schöning et al. *Letter of Intent for an Experiment to Search for the Decay $\mu \rightarrow eee$* . 2012.
- [2] U. Bellgardt et al. “Search for the Decay $\mu^+ \rightarrow e^+e^+e^-$ ”. In: *Nucl.Phys.* B299 (1988), p. 1. DOI: 10.1016/0550-3213(88)90462-2.
- [3] J. Beringer et al. (Particle data Group). In: *Phys. Rev. D* 86 010001 (2012). URL: <http://pdg.lbl.gov/>.
- [4] Y. Fukuda et al. “Evidence for Oscillation of Atmospheric Neutrinos”. In: *Phys. Rev. Lett.* 81 (8 1998), pp. 1562–1567. DOI: 10.1103/PhysRevLett.81.1562. URL: <http://link.aps.org/doi/10.1103/PhysRevLett.81.1562>.
- [5] Iro Maki, Masami Nakagawa, and Shoichi Sakata. “Remarks on the Unified Model of Elementary Particles”. In: *Progress of Theoretical Physics* 28.5 (1962), pp. 870–880.
- [6] H. E. Haber and G. L. Kane. “The Search for Supersymmetry: Probing Physics Beyond the Standard Model”. In: *Phys. Rept.* 117 (1985), p. 75.
- [7] M. Kiehn. “Track Fitting with Broken Lines for the MU3E Experiment”. PhD thesis. Heidelberg University, 2012.
- [8] DuPont High Performance Films, ed. *DuPont Kapton HN polyimide film*. 2011.
- [9] Autodesk Inc, ed. *Autodesk Simulation CFD 2013 material database*. 2012.
- [10] *435 Atmospheric Sampling. Theory and Calibration Procedures for the Use of a Rotameter*. Air Pollution Training Institute Training Course. Student Manuals. United States Environmental Protection Agency, 1983. URL: http://www.epa.gov/apti/Materials/APTI%20435%20student/Student%20Manual/Appendix_F_no%20TOC-cover_MRpf.pdf.
- [11] Wikipedia contributors. *Schematic rotameter front side*. Wikipedia - The Free Encyclopedia, 2006.
- [12] Andreas Schwarz, ed. *Royer Converter*. 2012. URL: http://www.mikrocontroller.net/articles/Royer_Converter.
- [13] ON Semiconductor, ed. *BUV27 NPN Silicon Power Transistor*. 2011.
- [14] JUMO GmbH & Co. KG, ed. *Platin-Chip-Temperatursensoren mit Anschlussdrähten nach DIN EN 60 751*. 90.6121. 2011, pp. 1–4.
- [15] JUMO GmbH & Co. KG, ed. *Aufbau und Anwendung von Platin-Temperatursensoren*. 90.6000.

- [16] U.Platt. *Master Course Environmental Physics (MKEP4)*. Lecture slides. Institut für Umweltphysik Heidelberg, Winter Term 2011/2012.
- [17] J.H. Lienhard. *A heat transfer textbook*. Phlogiston Press, 2003. Chap. 6. Laminar and turbulent boundary layers, pp. 271–315. ISBN: 9780971383524.
- [18] J. Christy and D. Balmer. *Fluid Mechanics 4*. Lecture notes. University of Edinburgh, 2003/2004. URL: <http://www.see.ed.ac.uk/~johnc/teaching/fluidmechanics4/2003-04/fluids2/node44.html>.
- [19] Wikipedia contributors. *Velocity profile of a laminar boundary layer created by a free stream flowing across a flat plate*. Wikipedia - The Free Encyclopedia, 2008.
- [20] J.H. Lienhard. *A heat transfer textbook*. Phlogiston Press, 2003. Chap. A. Some thermo-physical properties of selected materials, pp. 718–722. ISBN: 9780971383524.
- [21] Autodesk Inc., ed. *Energy Balance Discrepancies*. 2012. URL: <http://usa.autodesk.com/adsk/servlet/ps/dl/item?siteID=123112&id=17506169&linkID=18154757>.
- [22] C. J. Glassbrenner and Glen A. Slack. “Thermal Conductivity of Silicon and Germanium from 3°K to the Melting Point”. In: *Phys. Rev.* 134 (4A May 1964), A1058–A1069. DOI: 10.1103/PhysRev.134.A1058. URL: <http://link.aps.org/doi/10.1103/PhysRev.134.A1058>.
- [23] H.H. Binder. *Lexikon der chemischen Elemente: Das Periodensystem in Fakten, Zahlen und Daten*. S. Hirzel, 1999. ISBN: 9783777607368.

Acknowledgements

Zunächst möchte ich mich bei Prof. André Schöning dafür bedanken, dass er mir die Möglichkeit gegeben hat, diese Bachelorarbeit in seiner Arbeitsgruppe durchzuführen und mich in der Bearbeitungszeit inklusive der Schreibphase hervorragend betreut hat. Zudem gilt mein Dank Prof. Stephanie Hansmann-Menzemer für die Bewertung dieser Arbeit als Zweitprüferin.

Ich möchte mich zudem bei Dirk Wiedner und Sebastian Bachmann bedanken, da sie mir während der Bachelorarbeit immer mit Rat und Tat zur Seite standen. Mein Dank gilt auch allen anderen Mitgliedern der mu3e-Gruppe in Heidelberg, Niklaus Berger, Moritz Kiehn, Ann-Kathrin Perrevoort und Heiko Augustin, und den weiteren Mitgliedern in der Arbeitsgruppe von Herrn Schöning, für ihre Hilfsbereitschaft und die gute Arbeitsatmosphäre.

Außerdem gilt mein Dank Jens Wagner für die Unterstützung bei der Entwicklung der Induktionsheizung, Herrn Windelband für die Mithilfe beim Entwerfen des Kühlflusssaufbaus sowie Simon Rabenecker und Jessica Riedinger für die mechanische Umsetzung.

Außerdem möchte ich mich bei meinen Eltern für ihre Unterstützung während meines gesamten Bachelorstudiums bedanken.

A. LabView programming for temperature readout

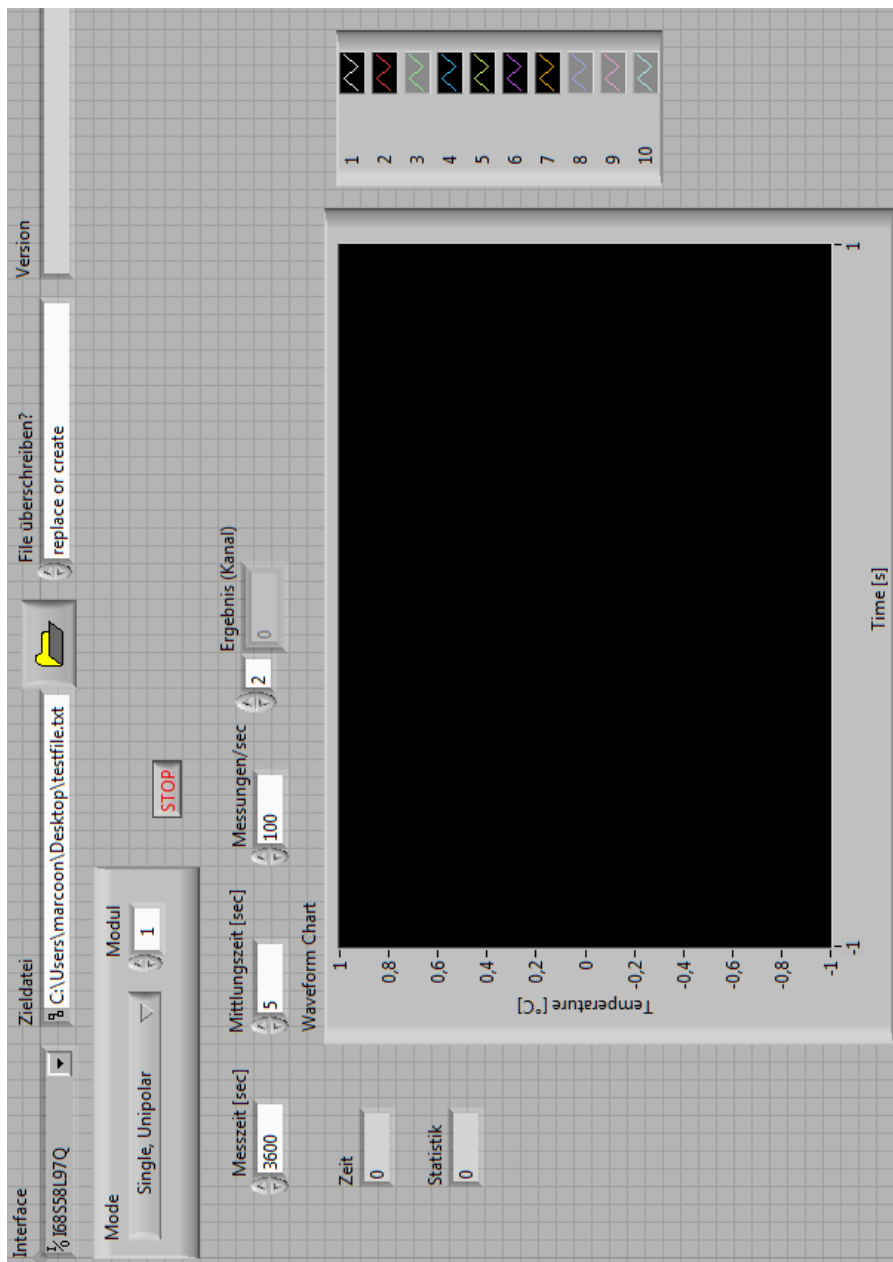


Figure A.1.
User interface of the used temperature readout program

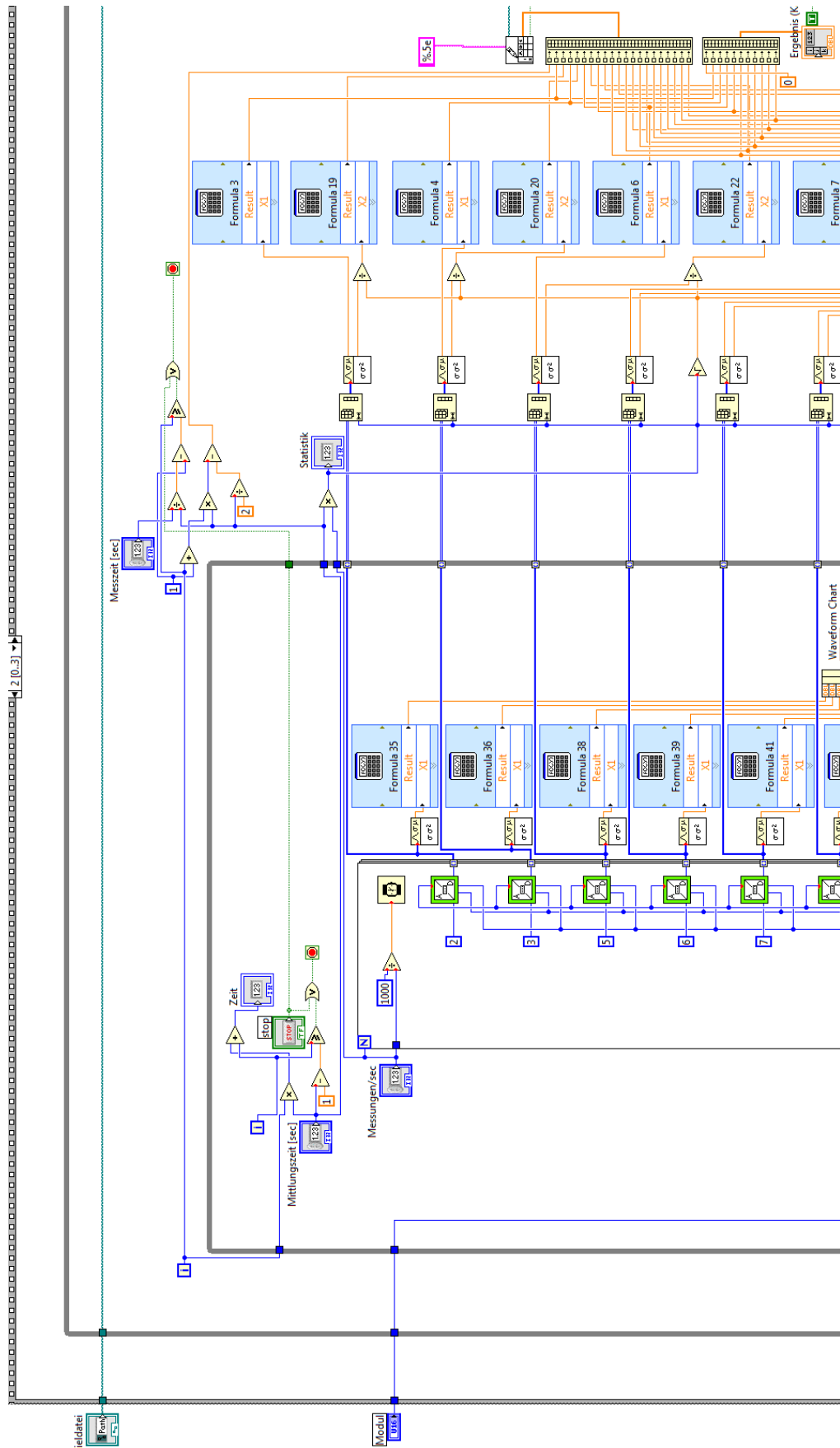


Figure A.2.
LabView programming (excerpt)

Erklärung

Ich versichere, dass ich diese Arbeit selbstständig verfasst und keine anderen als die angegebenen Quellen und Hilfsmittel benutzt habe.

Heidelberg, den 21. August 2012